Monthly Notices of the ROYAL ASTRONOMICAL SOCIETY

MNRAS **502,** 4743–4761 (2021) doi:10.1093/mnras/stab360
Advance Access publication 2021 February 10

A complete census of circumgalactic Mg II at redshift $z \lesssim 0.5$

Yun-Hsin Huang [1]★ Hsiao-Wen Chen [2] Stephen A. Shectman,[3] Sean D. Johnson [4] Fakhri S. Zahedy [3] Jennifer E. Helsby,[5] Jean-René Gauthier[6] and Ian B. Thompson[3]

[1]*Steward Observatory, University of Arizona, Tucson, AZ 85721, USA*
[2]*Department of Astronomy & Astrophysics, and Kavli Institute for Cosmological Physics, The University of Chicago, Chicago, IL 60637, USA*
[3]*The Observatories of the Carnegie Institution for Science, 813 Santa Barbara Street, Pasadena, CA 91101, USA*
[4]*Department of Astronomy, University of Michigan, 1085 S. University Ave, Ann Arbor, MI 48109, USA*
[5]*Freedom of the Press Foundation, 601 Van Ness Ave, San Francisco, CA 94102, USA*
[6]*Oracle Corporation, Redwood Shores, CA 94065, USA*

Accepted 2021 February 3. Received 2021 January 16; in original form 2020 December 2

ABSTRACT

This paper presents a survey of Mg II absorbing gas in the vicinity of 380 random galaxies, using 156 background quasi-stellar objects (QSOs) as absorption-line probes. The sample comprises 211 isolated (73 quiescent and 138 star-forming galaxies) and 43 non-isolated galaxies with sensitive constraints for both Mg II absorption and H α emission. The projected distances span a range from $d = 9$ to 497 kpc, redshifts of the galaxies range from $z = 0.10$ to 0.48, and rest-frame absolute B-band magnitudes range from $M_{\rm B} = -16.7$ to -22.8. Our analysis shows that the rest-frame equivalent width of Mg II, $W_r(2796)$, depends on halo radius ($R_{\rm h}$), B-band luminosity($L_{\rm B}$), and stellar mass ($M_{\rm star}$) of the host galaxies, and declines steeply with increasing d for isolated, star-forming galaxies. At the same time, $W_r(2796)$ exhibits no clear trend for either isolated, quiescent galaxies or non-isolated galaxies. In addition, the covering fraction of Mg II absorbing gas $\langle\kappa\rangle$ is high with $\langle\kappa\rangle \gtrsim 60$ per cent at <40 kpc for isolated galaxies and declines rapidly to $\langle\kappa\rangle \approx 0$ at $d \gtrsim 100$ kpc. Within the gaseous radius, the incidence of Mg II gas depends sensitively on both $M_{\rm star}$ and the specific star formation rate inferred from H α. Different from what is known for massive quiescent haloes, the observed velocity dispersion of Mg II absorbing gas around star-forming galaxies is consistent with expectations from virial motion, which constrains individual clump mass to $m_{\rm cl} \gtrsim 10^5\,{\rm M}_\odot$ and cool gas accretion rate of ~ 0.7–$2\,{\rm M}_\odot\,{\rm yr}^{-1}$. Finally, we find no strong azimuthal dependence of Mg II absorption for either star-forming or quiescent galaxies. Our results demonstrate that multiple parameters affect the properties of gaseous haloes around galaxies and highlight the need of a homogeneous, absorption-blind sample for establishing a holistic description of chemically enriched gas in the circumgalactic space.

Key words: surveys – galaxies: formation – galaxies: haloes – intergalactic medium – quasars: absorption lines.

1 INTRODUCTION

Over the past decades, extensive progress has been made to understand the impact of the baryon cycle on galaxy formation and evolution, with particular focus on gas reservoirs such as the circumgalactic medium (CGM). Located in the space between galaxies and the intergalactic medium (IGM), the CGM contains critical information on gas accretion and outflows, processes that drive the evolution of galaxies (see Chen 2017; Tumlinson, Peeples & Werk 2017, for recent reviews). Thus, the CGM provides an excellent laboratory for understanding the physical processes that drive the formation and evolution of galaxies.

Absorption-line spectroscopy of background quasars has provided a unique probe of the low-density CGM, which is otherwise too diffuse to be detected in emission beyond the local Universe. Over the last decade, statistically significant samples of galaxies at $z \approx$ 0–2 have been assembled using a combination of space- and ground-based telescopes. The Cosmic Origins Spectrograph (COS) on the *Hubble Space Telescope* (*HST*) has enabled studies of a rich suite of absorption lines including the H I Lyman series (e.g. Chen et al. 1998; Tripp, Lu & Savage 1998; Rudie et al. 2013; Tumlinson et al. 2013; Liang & Chen 2014; Werk et al. 2014; Borthakur et al. 2016), the O VI doublet (e.g. Chen & Mulchaey 2009; Prochaska et al. 2011; Tumlinson et al. 2011; Johnson, Chen & Mulchaey 2015a) and the C IV doublet (e.g. Borthakur et al. 2013; Bordoloi et al. 2014; Liang & Chen 2014).

From the ground, at $z \lesssim 2$ the majority of studies have focused on the measurement of the Mg II $\lambda\lambda$ 2796, 2803 doublets due to their strength and visibility in the optical range. This transition is thought to arise primarily in photoionized gas of temperature $T \sim 10^4$ K (Bergeron & Stasińska 1986; Charlton et al. 2003) and high neutral hydrogen column density clouds of $N({\rm H\,I}) \approx 10^{18}$–$10^{22}\,{\rm cm}^{-2}$ (Rao, Turnshek & Nestor 2006) for $W_r(2796)$ >0.3Å absorbers. Many investigations have been carried out to characterize the statistical properties of Mg II absorbers, including the frequency distribution function, redshift evolution of the absorber number density and kinematic signatures (e.g. Lanzetta, Turnshek & Wolfe 1987; Petitjean & Bergeron 1990; Charlton & Churchill 1998; Churchill et al. 2000; Churchill, Vogt & Charlton 2003; Nestor, Turnshek & Rao 2005).

★ E-mail: yunhsin@email.arizona.edu

Studies also show that Mg II absorbing gas probes the underlying gas kinematics around galaxies (e.g. outflow and inflow gas. Weiner et al. 2009; Kacprzak, Churchill & Nielsen 2012; Rubin et al. 2014; Ho et al. 2017; Ho & Martin 2020).

To have a comprehensive understanding of the baryonic structures around galaxies, significant progress has been made in constructing samples of galaxy–Mg II absorber pairs to understand the correlation between cool, enriched gas and galaxy properties. On the one hand, some galaxy–Mg II pair associations begin with quasar spectra and then search for nearby galaxies responsible for the Mg II absorption (e.g. Kacprzak et al. 2011). Such studies commonly target galaxies already known to have Mg II absorption in the spectra of background quasars and therefore may result in biased galaxy populations. On the other hand, studies have investigated relationships between galaxies and their surrounding gas using unbiased samples, where the galaxy–QSO (quasi-stellar object) pairs are chosen without any prior knowledge of the presence or absence of absorbing gas, allowing detailed studies of the CGM as a function of galaxy properties (including stellar mass, star formation rate, and colour) and environment (e.g. C10; Johnson, Chen & Mulchaey 2015b; Huang et al. 2016; Zahedy et al. 2016; Lan & Mo 2018; Martin et al. 2019).

As the Mg II doublet features start to be observable in the optical wavelengths at $z \sim 0.4$, this transition has not been studied as extensively at $z \lesssim 0.4$. Here, we make use of the ultraviolet (UV) sensitive spectrograph, the Magellan Echellette Spectrograph (MagE; Marshall et al. 2008), to perform searches for Mg II absorbers at redshifts as low as $z \sim 0.1$. Building upon the Sloan Digital Sky Survey (SDSS) data base, we conduct the Magellan MagE Mg II (M3) Halo Project in the spectra of background QSOs at $z \lesssim 0.4$. The main goal of the M3 Halo Project is to establish an unbiased, statistically significant sample of $z \lesssim 0.4$ Mg II absorbers to constrain the incidence, strength, and extent of Mg II absorbing gas around galaxies of different properties.

The first-year results of the M3 Halo Project are reported in Chen et al. (2010a, hereafter C10). With a spectroscopic sample of 94 galaxies at a median redshift of $\langle z \rangle = 0.24$ and projected distance $d \lesssim 170$ kpc, Chen et al. (2010a, b) investigated the possible correlations between the incidence and extent of Mg II absorbers and galaxy properties. We found the rest-frame equivalent width of Mg II ($W_r(2796)$) declines steeply with increasing d from the galaxies. Moreover, the extent of Mg II gaseous haloes scales strongly with the galaxy B-band luminosity and galaxy stellar masses, with slight dependence on specific star formation rate (sSFR) and no dependence on galaxy $B_{AB} - R_{AB}$ colour. The first-year results clearly demonstrate that Mg II absorbing gas is strongly connected to the physical properties of host galaxies. Using the full sample of the M3 Halo Project, we will show that we are able to observe a clear difference in surrounding gas properties between star-forming and quiescent galaxies.

The paper is organized as follows. In Section 2, we describe the experimental design of the M3 Halo Project, and the spectroscopic observations and data reduction of the photometrically selected galaxies and spectroscopically confirmed quasars in the SDSS archive. We present the catalogues of galaxies and Mg II absorbers in Section 3. In Section 4, we describe our likelihood analysis and characterize the correlation between Mg II absorption strength and galaxy properties. In Section 5, we discuss the covering fraction, the kinematics, and the azimuthal dependence of Mg II absorbing gas. We discuss the difference between different types of galaxies, the difference between isolated and non-isolated galaxies, and compare our results with previous studies. We present a summary of our findings in Section 6. We adopt the standard Λ cosmology, $\Omega_{\rm M} = 0.3$ and $\Omega_\Lambda = 0.7$ with a Hubble constant $H_0 = 70\,{\rm km\,s^{-1}\,Mpc^{-1}}$.

2 OBSERVATIONS

2.1 Experiment design

To investigate the correlation between galaxy properties and Mg II absorbing gas at small projected distances, we need to obtain spectroscopic data of both galaxies and QSO absorbers along common sightlines. We utilize the MagE (Marshall et al. 2008) on the Magellan Clay Telescope to conduct a survey of Mg II absorbers at $z < 0.4$. The high UV throughput of MagE from $\lambda = 3100$ Å enables searches of Mg II absorbers at redshift as low as 0.11. We refer the reader to C10 for a detailed description of the survey design. Briefly, the QSO and galaxy pairs are selected from the SDSS DR6 catalogues (Adelman-McCarthy et al. 2008). To maximize the efficiency of searching Mg II absorbers, we consider galaxies at photometric redshifts of $z_{\rm phot} \leq 0.4$ that have background QSOs in close projected distance $d < \hat{R}_{\rm gas}$. $\hat{R}_{\rm gas} = 130$ kpc is the distinct boundary found by Chen & Tinker (2008) using 23 galaxy–QSO pairs at intermediate redshifts of $z \sim 0.4$, beyond which no Mg II absorbers are found. Note that although we pre-select galaxy–QSO pairs with $d < \hat{R}_{\rm gas}$ for the spectroscopic follow-up survey, we also search the public SDSS DR14 sample (Abolfathi et al. 2018) to include galaxies with spectroscopic redshifts at $z \leq 0.4$ around our observed QSOs to study the gaseous halo beyond $\hat{R}_{\rm gas}$. Therefore, the properties of Mg II absorbing gas around galaxies are studied both within and beyond $\hat{R}_{\rm gas}$ in our survey. We reiterate that the galaxy–QSO pairs are chosen without any prior knowledge of the presence or absence of absorbing gas. In the following sections, we describe the galaxy spectroscopic sample either obtained from our own observations or SDSS DR14 archive and the observations of background quasars.

2.2 Galaxy spectroscopy

To establish a physical connection between galaxies and Mg II absorbing systems along nearby QSO sightlines, it is essential to have medium to high resolution spectra to obtain precise and accurate redshift measurements of these galaxies. We have obtained optical spectra of 218 galaxies that satisfy the criteria described above using the MagE Spectrograph (Marshall et al. 2008) at the Las Campanas Observatory and the Double Imaging Spectrograph (DIS; Lupton 1995) on the 3.5-m telescope at the Apache Point Observatory. Details about the spectroscopic observation setups and data reduction are presented in C10. In summary, we acquired 120 long-slit galaxy spectra using DIS over the period from 2008 August through 2010 September, and echellette spectra of 98 galaxies using MagE from 2008 August to 2011 March. The spectra obtained using DIS and MagE have intermediate resolution of full width at half-maximum (FWHM) $\lesssim 500\ {\rm km\,s^{-1}}$ and $\approx 150\ {\rm km\,s^{-1}}$ in the wavelength range between $\lambda \approx 4000$ Å and 1 μm. We reduced the DIS spectroscopic data using standard long-slit spectral reduction procedures, and the MagE spectra using the software developed by G. Becker with a slight modification to work with binned spectral frames. The redshifts of these galaxies were determined using a cross-correlation analysis with a linear combination of SDSS galaxy eigen spectra The typical redshift uncertainty is $\Delta z \sim 0.0003$ and 0.0001 for galaxy spectra taken using DIS and MagE.

We include 17 additional SDSS DR14 galaxies that already have reliable spectroscopic redshifts in the SDSS archive with projected distance $d < \hat{R}_{\rm gas}$ in our galaxy sample. We have also extended our search to $d < 500$ kpc in the SDSS archive and located 145 SDSS galaxies with accurate spectroscopic redshifts available. Combined with our own observations, we have a total of 380

Table 1. Summary of Faint Galaxy Spectroscopy.

ID	RA(J2000)	Dec(J2000)	$z_{\rm phot}$	r	Instrument	Exptime	UT Date
SDSSJ000548.29 − 084757.25	00:05:48.29	−08:47:57.25	0.25 ± 0.04	19.2	MagE	600	2009 Oct 19
SDSSJ000548.59 − 084801.16	00:05:48.59	−08:48:01.14	0.22 ± 0.07	19.4	MagE	300 + 600	2009 Oct 19
SDSSJ001335.12 + 141439.54	00:13:35.12	+ 14:14:39.55	0.26 ± 0.11	20.9	DIS	3 × 1800	2008 Dec 22
SDSSJ001336.14 + 141428.04	00:13:36.14	+ 14:14:28.01	0.25 ± 0.08	19.5	DIS	1800 + 1200	2008 Dec 22
SDSSJ003009.52 + 011445.25	00:30:09.52	+ 01:14:45.25	0.15 ± 0.02	17.7	SDSS	...	...
SDSSJ003009.90 + 011343.95	00:30:09.90	+ 01:13:43.95	0.53 ± 0.04	21.0	SDSS	...	...
SDSSJ003010.18 + 011219.92	00:30:10.18	+ 01:12:19.92	0.17 ± 0.03	18.5	SDSS	...	...
SDSSJ003012.84 + 011131.36	00:30:12.84	+ 01:11:31.36	0.08 ± 0.02	17.0	SDSS	...	...
SDSSJ003014.16 + 011359.19	00:30:14.17	+ 01:13:59.14	0.40 ± 0.11	20.8	DIS	1800	2009 Nov 9
SDSSJ003016.41 + 011406.90	00:30:16.41	+ 01:14:06.90	0.74 ± 0.05	21.2	SDSS	...	...

Note. The full table is available in the online version of the paper.

galaxies at $d < 500$ kpc in our final galaxy sample for searches of Mg II absorbers. A journal of the observations of the full galaxy sample is presented in Table 1.

2.3 Echellette spectra of QSOs

Echellete spectroscopic observations of 156 QSOs were obtained using the MagE spectrograph (Marshall et al. 2008) on the Magellan Clay telescope over the period from 2008 January through 2011 June. The majority of QSOs were observed using a 1 arcsec slit, yielding a typical spectral resolution of FWHM ≈ 70 km s^{-1}. All the QSO spectra were processed and reduced using the data reduction software developed by G. Becker. We refer the reader to C10 for details of observations and spectral reduction procedures. In brief, we first performed the wavelength and flux calibrations, and co-added the individual echellete orders to form a single contiguous spectrum across the spectral range from $\lambda = 3050$ Å to $\lambda = 1$ μm. The individual order-combined exposures were then continuum normalized and finally were stacked to form the final reduced spectrum. The signal-to-noise ratio e(S/N) per resolution element is $\gtrsim 10$ at wavelengths greater than ~ 3200 Å ($z \sim 0.14$), leading to a 2σ upper limit of $W_r(2796) \lesssim 0.13$ Å. For galaxies at lower redshifts, the error blows up and the S/N per resolution element can be as low as ∼3. We present a journal of the spectroscopic observations of the QSOs in Table 2.

3 THE GALAXY AND MG II ABSORBER CATALOGUES

3.1 Galaxy properties

We have constructed a full sample of 380 galaxies with robust redshift measurements in the vicinity of 156 distant background QSO sightlines. Among these galaxies, 103 galaxies are found to have at least one spectroscopic neighbour at projected distance $d \leq 500$ kpc and radial velocity difference Δv smaller than 1000 km s^{-1}. The presence of close neighbours implies that these galaxies are likely to reside in a group environment, where the interactions of group members may change the correlation between galaxy properties and their gaseous haloes. We also performed a literature search and identified nine galaxies that are either previously known merging systems, galaxy groups or clusters (e.g. Koester et al. 2007; Hao et al. 2010; Smith et al. 2012; Johnson et al. 2014). To avoid the confusion of associating Mg II absorbers with host galaxies, we classify these galaxies as 'non-isolated' galaxies and discuss them separately. The criteria yielded a sample of 277 'isolated' galaxies and 103 'non-isolated' galaxies.

We first present the projected distance d versus redshift distribution of the full galaxy sample in Fig. 1. The isolated and non-isolated galaxies are presented in solid and open symbols. The redshifts of the galaxies range from $z = 0.08$ to $z = 0.83$ with a median of $<z> = 0.22$. Using our own DIS and MagE observations, we measure redshifts of 218 galaxies and find that the SDSS photometric redshift measurements are accurate to within a median residual of $<|(z_{\rm phot} - z_{\rm spec})/(1 + z_{\rm spec})| > = 0.05$ with an rms scatter of $\delta z \equiv \Delta z/(1 + z) = 0.07$. We find that 91 per cent of galaxies (198 out of 218) have redshifts at $z = 0.1$–0.4, showing that the target selection based on photometric redshifts is effective in identifying foreground galaxies at our targeted redshift range.

For our own observations, the projected distances of the QSOs range from $d \approx 9$–178 kpc with a median of $<d> = 48$ kpc. 18 per cent (39 out of 218) galaxies have projected distance $d > \hat{R}_{\rm gas}$, and only one galaxy has $d > 1.5\,\hat{R}_{\rm gas}$, showing that our QSO–galaxy pair selection effectively probes properties of gaseous haloes close to the host galaxies. The SDSS galaxies occupy predominantly the regime of large projected distances, where 40 galaxies have $d \leq 1.5\,\hat{R}_{\rm gas}$ and the remaining 122 galaxies extend out to $d = 497$ kpc. The full galaxy sample has $d \approx 9$–497 with a median of $<d> = 94$ kpc. In Fig. 1, we also adopt various colours and symbols to highlight different ranges of galaxy luminosity. We estimate a B-band luminosity for each galaxy following the steps in C10, and find that the full galaxy sample spans a wide range of B-band luminosity. The sample has 200 luminous galaxies ($L_{\rm B} > L_{\rm B_*}$) spanning a range in their projected distance to a QSO sightline from $d = 11$ kpc to $d = 497$ kpc, and 169 sub-L_* galaxies ($L_{\rm B} = 0.1$–$1\,L_{\rm B_*}$) covering a range from $d = 12$ kpc to $d = 494$ kpc. The sample also includes 11 low-luminosity dwarf galaxies with $L_{\rm B} < 0.1\,L_{\rm B_*}$ from $d = 9$ kpc to $d < 293$ kpc.

While B-band luminosity is known to scale with halo mass (e.g. Yang et al. 2005; Tinker et al. 2007), it is also found to correlate with [O II] luminosity despite a large scatter (Zhu, Moustakas & Blanton 2009). To have a more robust tracer of dark matter halo mass, we also calculate the total stellar mass $M_{\rm star}$ (More et al. 2011) and Hα equivalent width as an indicator of star formation. We estimate the stellar mass according to Johnson et al. (2015a, equations 1 and 2). Briefly, they use low-redshift galaxies of $z < 0.055$ in the NASA-Sloan Atlas (e.g. Maller et al. 2009) to derive the relation between stellar mass and rest-frame g- and r-band absolute magnitudes. The relation can well reproduce the NASA-Sloan Altas stellar masses with a systematic error of less than 0.02 dex and a 1σ scatter of less than 0.15 dex over the entire range of our galaxy absolute r-band magnitudes. They also show that the systematic error induced by the redshift evolution of the mass-to-light ratio relation for $z = 0.1$–0.4 galaxies is less than 0.1 dex. We estimate the rest-frame g- and r-

Table 2. Summary of the MagE spectroscopic observations of SDSS QSOs.

ID	RA(J2000)	Dec(J2000)	z_{QSO}	u'	Exptime	UT Date
SDSSJ000548.24 − 084808.44	00:05:48.24	−08:48:08.44	1.19	17.96	2 × 1200	2009 Oct 19
SDSSJ001335.75 + 141424.07	00:13:35.75	+ 14:14:24.07	1.54	19.32	1800 + 1300	2009 Oct 20
SDSSJ003013.91 + 011405.14	00:30:13.91	+ 01:14:05.14	1.46	18.12	2 × 1800	2010 Jul 13
SDSSJ003340.21 − 005525.53	00:33:40.21	−00:55:25.53	0.94	17.99	2 × 900	2008 Sep 23
SDSSJ003407.35 − 085452.12	00:34:07.35	−08:54:52.12	1.31	18.59	2 × 1200	2008 Sep 24
SDSSJ003413.04 − 010026.86	00:34:13.04	−01:00:26.86	1.29	17.33	2 × 600	2008 Sep 23
SDSSJ010135.84 − 005009.08	01:01:35.84	−00:50:09.08	1.01	19.31	2 × 1800	2008 Sep 24
SDSSJ010156.32 − 084401.74	01:01:56.32	−08:44:01.74	0.98	18.29	2 × 1800	2008 Sep 25
SDSSJ010205.89 + 001156.99	01:02:05.89	+ 00:11:56.99	0.72	17.59	1500 + 900	2009 Oct 18
SDSSJ010352.47 + 003739.79	01:03:52.47	+ 00:37:39.79	0.70	18.36	3 × 1200	2008 Sep 25

Note. The full table is available in the online version of the paper.

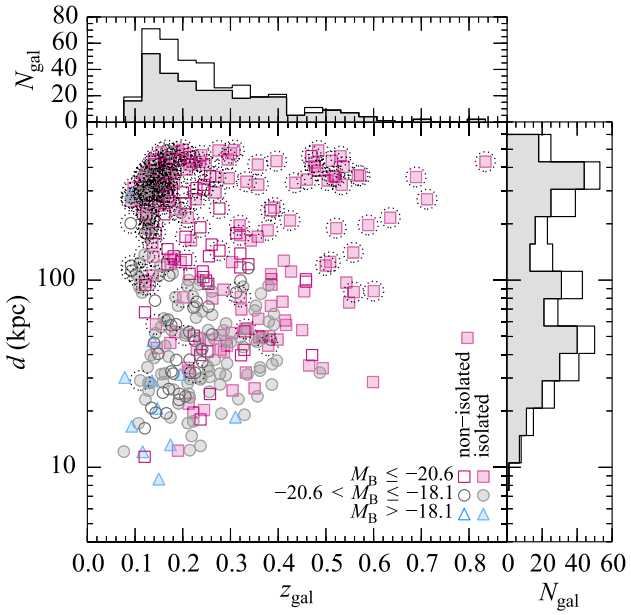

Figure 1. Distribution of projected distance d versus redshift for 277 isolated galaxies (solid symbols) and 103 galaxies in the 'non-isolated' sample (open symbols). We show luminous galaxies of $L_B > L_{B*}$ in magenta squares, sub-L∗ galaxies of $L_B = (0.1\text{–}1)\,L_{B*}$ in grey circles, and low-luminosity galaxies of $L_B < 0.1\,L_{B*}$ in cyan triangles. Galaxies with spectroscopic redshifts from SDSS are marked in dotted circles. The *top* and *right-hand* panels show, respectively, the redshift and projected distance histograms of the full sample (open histograms) and the isolated galaxy sample (filled histograms).

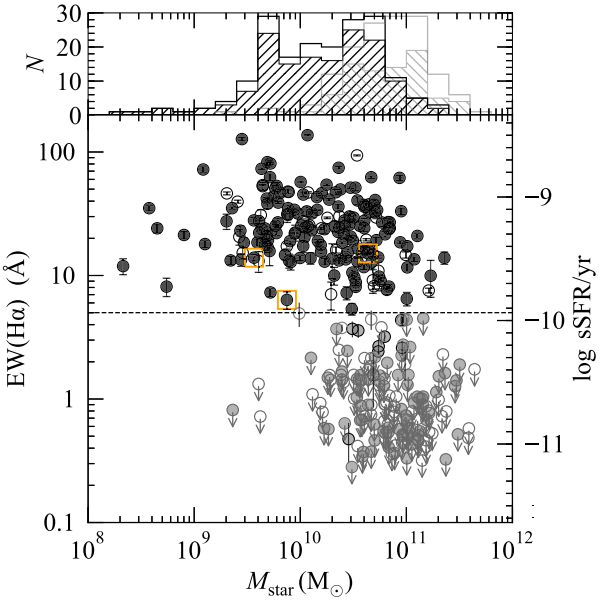

Figure 2. Correlation between rest-frame Hα equivalent width and stellar mass. Filled and open circles represent respectively the isolated and non-isolated galaxies. Galaxies likely to be dominated by an AGN are marked in orange squares. Non-detections are shown as 2σ upper limits marked by light grey points with downward arrows. The vertical errors represent 1σ uncertainties. The division between star-forming and quiescent galaxies is shown as horizontal dashed line (EW(Hα)=5Å). Galaxies with 2σ upper limits greater than EW(Hα) = 5Å do not have the sensitivity to distinguish between star-forming and quiescent galaxies. They are not displayed and are excluded in our final sample.

band absolute magnitudes by interpolation of observed SDSS g, r, i, z bands. For fainter galaxies with $\leq 5\sigma$ detection in g-band absolute magnitude, we calculate the stellar mass using the relation between stellar mass and single rest-frame r-band magnitude in Liang & Chen (2014), which is also derived using the NASA-Sloan Atlas sample.

We measure the equivalent width of the Hα emission line for each galaxy spectrum, adopting the window definitions from Yan et al. (2006). The stellar mass as a function of Hα equivalent width, EW(Hα), is presented in Fig. 2. We also show on the right axis the inferred specific star-formation rate (sSFR) following equations (2) and (4) in Fumagalli et al. (2012). We mark cyan squares around galaxies likely to be dominated by an AGN (active galactic nucleus), based on the classification scheme derived by Kewley et al. (2001) with the optical line ratios N II/Hα and [O III]/Hβ. We find that there seems to be a clear distinction at EW(Hα) $\approx$ 5 Å. Below EW(Hα) = 5 Å, only 15 out of 146 galaxies (10 per cent) have detected Hα emission at a 2σ level. At EW(Hα) >5 Å, most galaxies (98 per cent) have detected Hα, except for three galaxies with low S/N spectra. We therefore divide our galaxies into 'star-forming' and 'quiescent' galaxy samples using the criterion of whether their EW(Hα) are greater than 5 Å. A total of 327 out of 380 galaxies have high enough S/N measurements on the Hα emission, where 184 (143) are classified as star-forming (quiescent) galaxies. The cut essentially limits our galaxy sample to $z \lesssim 0.5$, beyond which the observed Hα emission is red-shifted to $\gtrsim 1\,\mu$m and falls outside of the wavelength range of the optical spectrographs. We find that our full sample spans a wide range in stellar mass, from $M_{star} = 2 \times 10^8\,M_\odot$ to $M_{star} = 4 \times 10^{11}\,M_\odot$ with a median $\langle M_{star} \rangle = 4 \times 10^{10}\,M_\odot$. The star-forming galaxies have lower stellar mass from $\log M_{star}/M_\odot = 8.3\text{–}11.4$ with a median of $\log M_{star}/M_\odot =$

Table 3. Galaxies and absorption systems.

	Galaxies									Absorption systems	
ID	$\Delta\alpha$ (arcsec)	$\Delta\delta$ (arcsec)	z_{gal}	d (kpc)	r'	M_B	log $M_{star}/M_\odot$	R_h (kpc)	EW(H α) (Å)	z_{abs}	$W(2796)$ (Å)
(1)	(2)	(3)	(4)	(5)	(6)	(7)	(8)	(9)	(10)	(11)	(12)
SDSSJ001336.14 + 141428.04	5.8	3.9	0.1910	21.9	19.52	−19.93	9.7	143.9	20.8 ± 1.2	0.1908	1.30 ± 0.13
SDSSJ003009.52 + 011445.25	− 65.9	40.1	0.1845	238.7	17.72	−21.51	10.7	247.7	40.9 ± 0.7	0.1845	< 0.10
SDSSJ003010.18 + 011219.92	− 55.9	− 105.2	0.1501	311.6	18.48	−20.14	10.4	200.6	49.7 ± 0.4	0.1501	< 0.13
SDSSJ003014.16 + 011359.19	3.9	− 6.0	0.2125	24.7	20.81	−18.59	9.7	142.9	19.4 ± 4.0	0.2126	0.37 ± 0.05
SDSSJ003339.86 − 005522.39	− 5.4	3.3	0.2124	21.9	18.99	−20.79	9.8	149.0	46.7 ± 2.9	0.2121	1.05 ± 0.03
SDSSJ003406.33 − 085448.74	− 15.4	3.4	0.1403	38.5	18.04	−20.18	10.6	228.1	< 0.7	0.1403	< 0.14
SDSSJ003407.78 − 085453.28	6.5	− 1.1	0.3617	32.8	21.59	−19.43	9.8	134.7	50.7 ± 3.0	0.3616	0.48 ± 0.05
SDSSJ003411.94 − 005808.52	− 16.5	138.3	0.1539	372.2	19.20	−19.77	9.7	149.0	80.7 ± 1.4	0.1539	< 0.14
SDSSJ003412.85 − 010019.81	− 2.9	7.1	0.2564	30.4	20.08	−19.79	10.3	184.1	< 3.7	0.2564	0.61 ± 0.06
SDSSJ003414.49 − 005927.51	21.8	59.3	0.1202	136.9	17.27	−20.54	10.7	267.4	< 1.4	0.1212	< 0.21
non-isolated Galaxies											
SDSSJ000548.29 − 084757.25	0.7	11.2	0.3293	53.2	19.21	−21.45	11.0	297.9	1.9 ± 0.5	0.3288	0.11 ± 0.02
SDSSJ000548.59 − 084801.16	5.2	7.3	0.3293	42.4	19.43	−21.22	10.8	251.4	< 0.6	...	...
SDSSJ003339.66 − 005518.39	− 8.2	7.2	0.1760	32.5	19.66	−18.96	10.1	172.4	< 1.1	0.1759	0.19 ± 0.04
SDSSJ003341.48 − 005522.82	19.1	2.8	0.1758	57.4	20.79	−18.32	9.4	133.1	20.6 ± 3.0	...	...
SDSSJ003357.90 − 085356.03	− 141.7	56.1	0.1381	367.9	17.76	−20.50	10.6	235.0	< 0.7	0.1381	< 0.22
SDSSJ010133.65 − 005028.98	− 32.9	− 19.9	0.2605	154.9	17.98	−21.97	11.2	409.4	< 0.8	0.2605	< 0.10
SDSSJ012557.41 − 000749.58	− 83.7	32.9	0.2574	359.3	18.66	−21.20	11.0	302.5	< 0.4	0.2569	0.79 ± 0.04
SDSSJ012603.20 − 000827.82	3.2	− 5.3	0.2571	24.6	18.55	−21.44	10.8	255.4	< 1.5	...	...
SDSSJ020111.79 − 002537.67	− 26.1	106.3	0.1568	296.8	19.44	−19.46	9.9	158.1	47.7 ± 1.6	...	...
SDSSJ020117.91 − 002559.59	65.8	84.4	0.1577	291.5	18.97	−19.63	10.3	189.6	< 1.4	...	...
SDSSJ020119.90 − 002831.16	95.5	− 67.2	0.1602	322.4	17.83	−20.75	10.8	271.5	< 0.7	0.1602	< 0.15

*Note.*The full table is available in the online version of the paper.

10.3, while the quiescent galaxy sample has higher stellar mass from log $M_{star}/M_\odot$ = 9.3–11.6 with a median of log $M_{star}/M_\odot$ = 10.8.

3.2 Absorber properties

For each galaxy in our sample, we searched for the corresponding Mg II absorption doublet in the echellette spectra of the background QSO within a radial velocity difference $\Delta v = \pm 1000$ km s^{-1} of the galaxy redshift. When a Mg II absorber was identified, we measured its rest-frame equivalent width and associated error by direct integration over the line region in our continuum normalized spectrum. We accepted the absorption lines according to a 2σ detection threshold, which is appropriate since the searches are performed at known galaxy redshifts. We then determined the absorber redshift based on the best-fitting line centroid of a Gaussian profile analysis of Mg II λ2796. In cases where no Mg II features are detected, we placed 2σ upper limits on the Mg II λ2796 equivalent widths. For 'non-isolated' systems, we calculate the luminosity-weighted projected position and redshift using members in each system and obtain its associated absorber properties following the same procedure.

In summary, the procedure yielded 85 physical galaxy–Mg II pairs and 126 upper limits in the vicinities of 211 isolated galaxies, and 18 Mg II absorbers and 25 upper limits around 43 'non-isolated' systems. We were not able to obtain significant constraints for Mg II absorption equivalent widths around 14 galaxies and two 'non-isolated' systems, where the expected QSO spectra are contaminated by other strong absorption features (e.g. C IV λλ 1548, 1550) or the atmosphere O3 absorption complex at λ ≈ 3200. Also, six galaxies and two 'non-isolated' systems were found at spectroscopic redshifts $z_{spec} \lesssim 0.09$, falling outside the wavelength range of the MagE spectrograph. We present the properties of each spectroscopically confirmed galaxy sample in Table 3 (Columns 1–10), and the associated redshift and absorption equivalent width of Mg II absorbers in Columns 11 and 12 of Table 3.

The final isolated galaxy–absorber pair sample spans a projected distance range of d = 9–497 kpc with a median of $\langle d \rangle_{med}$ = 73 kpc. The redshifts of the isolated galaxies range from z = 0.10–0.48 with a median of $\langle z \rangle_{med}$ = 0.21, and the rest-frame absolute B-band magnitudes range from $M_B = -16.7$ to $M_B = -22.8$ with a median of $\langle M_B \rangle_{med} = -20.5$. The 'non-isolated' systems span a redshift range of z = 0.12–0.47 with a median of $\langle z \rangle_{med}$ = 0.19, with projected distance from d = 11–446 kpc with a median of $\langle d \rangle_{med}$ = 128 kpc.

We examine the relative velocity distribution of Mg II absorbers with respect to the systematic redshifts of the galaxies. In the left-hand panel of Fig. 3, we present the velocity dispersion of the detected Mg II absorbing gas around the full galaxy–absorber pair sample. We also show the velocity dispersion separately for isolated and non-isolated galaxy–absorber pairs in the central and right-hand panels of Fig. 3. We characterize the velocity distribution using a Gaussian profile with iterative 3σ clipping to exclude outliers. The velocity distribution of Mg II absorbing gas around galaxies can be characterized by a single Gaussian distribution of mean velocity difference $\langle v_{\rm Mg\,II\text{-}Galaxy} \rangle$ = 0 km s^{-1} and dispersion σ_v = 84 km s^{-1} (left-hand panel of Fig. 3), while the velocity distribution for isolated galaxies is best represented by a Gaussian profile centred at $\langle v_{\rm Mg\,II\text{-}Galaxy} \rangle = -4$ km s^{-1} and σ_v = 80 km s^{-1}. For 'non-isolated' systems, we find the associated Mg II absorbers have a broad velocity distribution with a standard deviation of $\sigma_{v,std}$ = 235 km s^{-1}.

We present in Fig. 4 the correlation between the strength of Mg II absorption and galaxy projected distance. Following the presentation in Fig. 3, we show the distributions separately for isolated and non-isolated galaxies to investigate the influence of galaxy environment. Similar to previous surveys (e.g. C10), we find a clear trend of decreasing absorption strength with increasing projected distance for isolated galaxies (see the middle panel of Fig. 4). Beyond

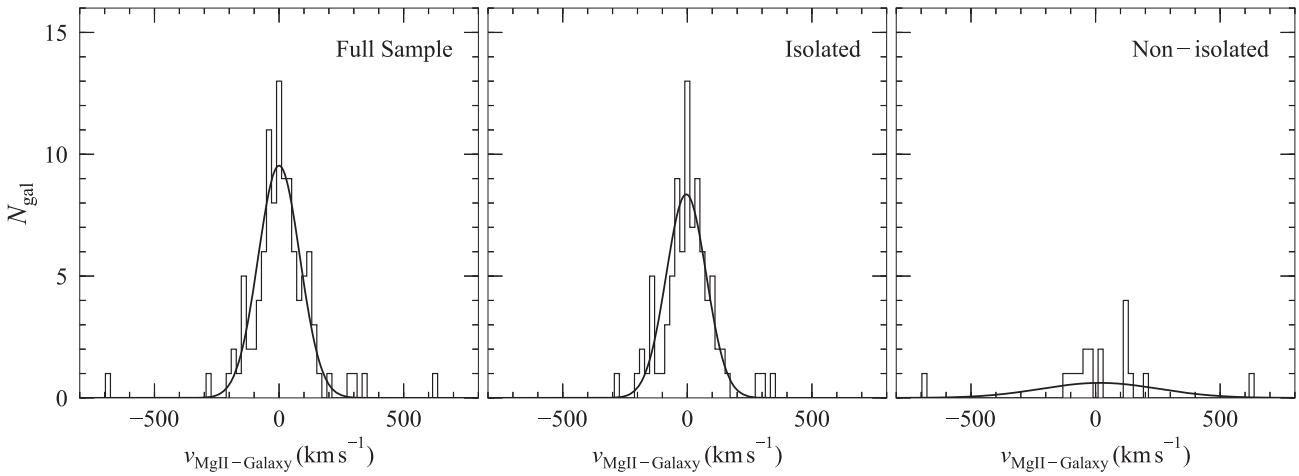

Figure 3. Relative velocity distributions of Mg II absorbers with respect to the galaxy systematic redshifts. The full galaxy sample is shown in the left-hand panel and is separated into isolated and non-isolated galaxy samples in the middle and right-hand panels. We detect associated Mg II absorbers in 103 out of 211 isolated galaxies and 18 out of 43 group systems searched. We characterize each relative velocity distribution by a single Gaussian profile (solid curve in each panel), excluding outliers according to an iterative 3σ clipping. The full galaxy sample is well characterized by a Gaussian distribution with a mean velocity difference $\langle v_{\rm Mg\ II\text{-}Galaxy}\rangle = 0$ km s^{-1} and dispersion of $\sigma = 84$ km s^{-1} (left-hand panel). While adopting a Gaussian profile to characterize the velocity distribution of Mg II gas around isolated (non-isolated) galaxies leads to a Gaussian profile centred at $\langle v_{\rm Mg\ II\text{-}Galaxy}\rangle = -4(17)$ km s^{-1} and $\sigma = 80\,(235)$ km s^{-1}. Since only 18 systems are in the non-isolated sample, we also calculate the standard deviation of the velocity dispersion to be $\sigma_{v,\rm std} = 235$ km s^{-1}, consistent with what we obtain using the Gaussian profile fitting. Note that for non-isolated systems, the galaxy systematic redshift is defined as the luminosity-weighted redshift of member galaxies.

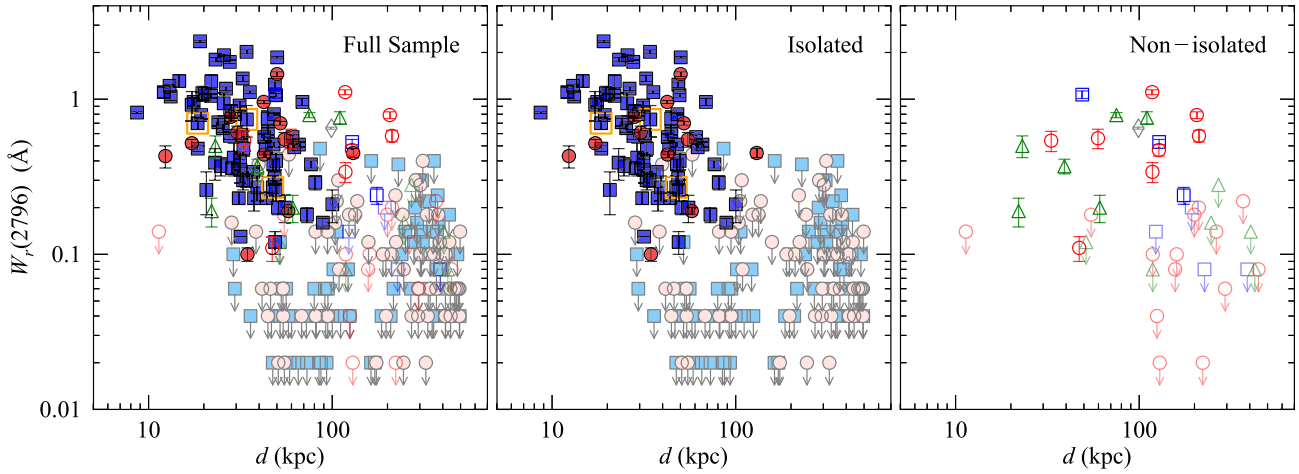

Figure 4. Rest-frame absorption equivalent width $W_r(2796)$ versus projected distance d for the full (left), isolated (middle; filled symbols) and non-isolated (right; open symbols) galaxy samples. Star-forming and quiescent galaxies are shown in blue squares and red circles, respectively. Galaxies likely to be dominated by an AGN are marked in orange squares. Galaxies with detected Mg II absorbers are shown in solid symbols with error bars representing measurement uncertainties. Non-detections are displayed as 2σ upper limits (points with downward arrows) and lighter colouring. Note that for non-isolated systems, we use the luminosity-weighted projected distance as d and display a single data point for each system. Non-isolated systems that contain both star-forming and quiescent galaxies are shown in green triangles. We display in grey diamonds for non-isolated systems which we cannot determine whether their member galaxies are star-forming or quiescent.

70 kpc, no Mg II absorbing gas with $W_r(2796) > 0.5$ Å is found, and no detections are present beyond projected distance $d \gtrsim 150$ kpc ($d \geq \hat{R}_{\rm gas}$). In contrast, while non-isolated systems do have lower Mg II covering fraction at larger projected distance d, we do not find a clear anticorrelation between the $W_r(2796)$ and d. The strong Mg II absorbers of $W_r(2796) \sim 0.5$ Å are detected out to 150 kpc. Note that using the projected distance of the nearest galaxy in non-isolated systems as d does not change the lack of anticorrelation in the $W_r(2796)$ versus d plot.

To determine whether the recent star formation of galaxies has an impact on Mg II absorbing gas, we further divide the isolated galaxy sample into star-forming and quiescent galaxy samples and show the distributions of $W_r(2796)$ versus projected distance in the upper panels of Fig. 5. While both galaxy samples appear to occupy a similar $W_r(2796)$ versus d space, qualitatively the star-forming galaxies show strong inverse correlation whereas only a modest trend is revealed for quiescent galaxies.

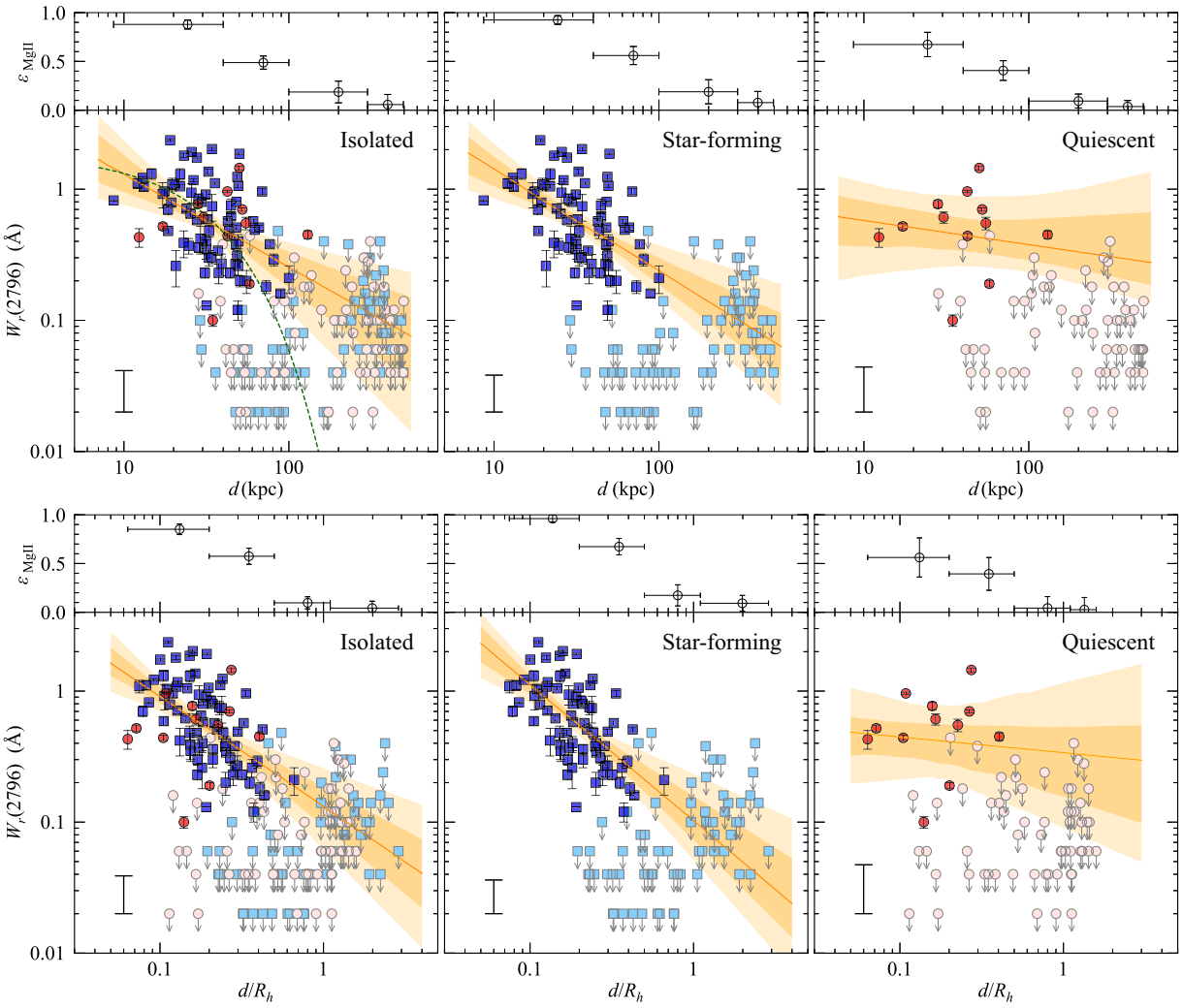

Figure 5. Rest-frame equivalent width $W_r(2796)$ versus projected distance d (upper panels) and $R_{\rm h}$-normalized projected distance $d/R_{\rm h}$ (lower panels). The full isolated galaxy sample is shown in the left-hand panels, and is separated into isolated star-forming and quiescent galaxy samples in the middle and right-hand panels. Symbols are the same as in Fig. 4. The orange solid lines represent the best-fitting power-law models. The dark and light shaded bands represent the 68 per cent and 95 per cent confidence intervals from the MCMC realizations. The best-fitting intrinsic scatter is marked in the lower left corner. At the top of each panel, we show the best-fitting results of the four non-parametric mean covering fractions from the maximum likelihood analysis. The horizontal bars mark the full range of projected distance within each bin and vertical error bars represent the 68 per cent confidence interval. The best-fitting models are discussed in equations (6)−(11) and in the text. For comparison, the green dashed curve in the upper left panel shows the log-linear maximum likelihood fit from Nielsen, Churchill & Kacprzak (2013b).

4 ANALYSIS

In the previous section, we use the samples of 211 isolated galaxies (73 quiescent galaxies and 138 star-forming galaxies) and 43 non-isolated galaxies to show that the strength and incidence of Mg II absorbing gas appear to depend on galaxy properties. In this section, we quantify the correlation between $W_r(2796)$ and different galaxy properties. We obtain and assess various models that well describe the data and present the best-fitting results.

4.1 Fitting procedure and model evaluation

We perform a likelihood analysis to obtain the best-fitting models and to better characterize the correlation between galaxy properties and Mg II absorbers. The generalized functional form to describe the mean Mg II absorption equivalent width $\bar{W}_r(2796)$ is

$$\bar{W}_r(2796) = f(x_1, x_2, ...), \quad (1)$$

where x_i's are independent measurements of galaxy properties including projected distance (d), rest-frame absolute B-band luminosity ($M_{\rm B}$) and stellar mass ($M_{\rm star}$). We adopt a simple power-law profile to describe the correlation between $W_r(2796)$, d and other properties. In logarithmic space, the model is expressed as a linear equation

$$\log \bar{W}_r(2796) = a_0 + a_1 \log d + a_2 X + ... \quad (2)$$

In addition, we introduce a non-parametric covering fraction ϵ in the model to describe the clumpy nature of Mg II gaseous haloes. This is motivated by our findings that the covering fraction of Mg II absorbing gas may be less than unity and varying at different projected distances. As shown in Fig. 4, a non-negligible fraction of galaxies at small projected distances ($d \lesssim 40$ kpc) do not give

Table 4. Summary of maximum likelihood solutions.

Model I	a_0	a_1	a_2	σ_c	$\epsilon_1[0, 40]^{(a)}$	$\epsilon_2[40, 100]$	$\epsilon_3[100, 300]$	$\epsilon_4[300, 700]$	Kendall's τ
full	0.83 ± 0.38	-0.72 ± 0.25	...	0.32 ± 0.04	0.87 ± 0.05	0.49 ± 0.06	0.19 ± 0.12	0.06 ± 0.06	-0.46 ± 0.04
blue	0.94 ± 0.30	-0.78 ± 0.20	...	0.28 ± 0.03	0.92 ± 0.05	0.56 ± 0.09	0.19 ± 0.12	0.08 ± 0.08	-0.52 ± 0.05
red	-0.08 ± 0.34	-0.17 ± 0.20	...	0.34 ± 0.06	0.67 ± 0.11	0.41 ± 0.10	0.09 ± 0.07	0.04 ± 0.04	-0.22 ± 0.05
Model II	a_0	a_1	a_2	σ_c	$\epsilon_1[0, 0.2]$	$\epsilon_2[0.2, 0.5]$	$\epsilon_3[0.5, 1.1]$	$\epsilon_4[1.1, 4]$	Kendall's τ
Rh-full	-0.88 ± 0.15	-0.84 ± 0.20	...	0.29 ± 0.03	0.85 ± 0.06	0.57 ± 0.08	0.10 ± 0.06	0.07 ± 0.07	-0.45 ± 0.04
Rh-blue	-0.98 ± 0.17	-1.03 ± 0.22	...	0.26 ± 0.03	0.95 ± 0.04	0.67 ± 0.08	0.18 ± 0.10	0.12 ± 0.12	-0.55 ± 0.05
Rh-red	-0.48 ± 0.27	-0.12 ± 0.24	...	0.37 ± 0.09	0.53 ± 0.18	0.39 ± 0.15	0.07 ± 0.07	0.05 ± 0.05	-0.21 ± 0.05
Model III	a_0	a_1	a_2	σ_c	$\epsilon_1[0, 40]$	$\epsilon_2[40, 100]$	$\epsilon_3[100, 300]$	$\epsilon_4[300, 700]$	Kendall's τ
MB-full	1.22 ± 0.25	-0.94 ± 0.16	-0.09 ± 0.03	0.28 ± 0.03	0.95 ± 0.04	0.58 ± 0.09	0.11 ± 0.07	0.04 ± 0.04	-0.47 ± 0.04
MB-blue	1.57 ± 0.28	-1.14 ± 0.18	-0.12 ± 0.02	0.25 ± 0.03	0.97 ± 0.02	0.60 ± 0.08	0.18 ± 0.11	0.05 ± 0.05	-0.56 ± 0.05
MB-red	0.09 ± 0.33	-0.27 ± 0.20	-0.02 ± 0.05	0.34 ± 0.06	0.54 ± 0.17	0.37 ± 0.17	0.07 ± 0.07	0.03 ± 0.03	-0.23 ± 0.05
Model IV	a_0	a_1	a_2	σ_c	$\epsilon_1[0, 40]$	$\epsilon_2[40, 100]$	$\epsilon_3[100, 300]$	$\epsilon_4[300, 700]$	Kendall's τ
Mstar-full	1.35 ± 0.25	-1.05 ± 0.17	0.21 ± 0.08	0.28 ± 0.03	0.85 ± 0.06	0.53 ± 0.07	0.10 ± 0.07	0.07 ± 0.07	-0.46 ± 0.04
Mstar-blue	1.42 ± 0.22	-1.07 ± 0.14	0.28 ± 0.06	0.27 ± 0.02	0.97 ± 0.03	0.64 ± 0.08	0.17 ± 0.09	0.02 ± 0.02	-0.56 ± 0.05
Mstar-red	0.01 ± 0.36	-0.24 ± 0.21	0.01 ± 0.03	0.38 ± 0.04	0.50 ± 0.16	0.26 ± 0.12	0.08 ± 0.06	0.09 ± 0.09	-0.22 ± 0.05

$^{(a)}\epsilon_i\ [d_1, d_2]$ represents the mean covering fraction within $[d_1, d_2]$ in d or normalized d.

rise to Mg II absorption to sensitive upper limits, and we find an increasing fraction of upper limits at larger projected distances. We divide the mean covering fraction ϵ_k ($k = 1$–4) into four projected distance intervals. To obtain a better sampling of ϵ at small projected distances, the first two bins ($k = 1, 2$) are designed for d $\lesssim 100$ kpc, where most Mg II absorbers are found. The other two bins ($k = 3$, 4) are used for larger projected distances, each with a roughly equal number of galaxies.

Here, we perform the maximum likelihood analysis to determine the values of coefficients a_i and four mean covering fractions that best represent the data. The likelihood function is defined as

$$\mathscr{L} = \prod_{i=1}^{n} \left\{(\epsilon|d_i)g_i + [1 - (\epsilon|d_i)]h_i\right\}, \tag{3}$$

where g_i represents the probability density function that the QSO sightline intercepts the Mg II gas around galaxy and its strength ($W_r(2796)$) follows the underlying power-law model, and h_i denotes the probability density function (pdf) that the QSO sightline does not intercept any Mg II gas around galaxy i. Here, $\langle\epsilon|d_i\rangle$ is the non-parametric mean covering fraction given the projected distance of galaxy i (d_i). The two probability density functions g_i and h_i are weighted according to the mean covering fraction $(\epsilon|d_i)$ and combined to get the likelihood function of a single galaxy i.

The first probability density function g_i is expressed as

$$g_i = \int_0^\infty \mathrm{d}W' \left(\frac{1}{\sqrt{2\pi}\ W'\ \sigma_{\rm insc}} \exp\left\{-\frac{1}{2}\left[\frac{\ln(W') - \ln(\bar{W})}{\sigma_{\rm insc}}\right]^2\right\}\right) \times \left(\frac{1}{\sqrt{2\pi}\sigma_i} \exp\left\{-\frac{1}{2}\left(\frac{W' - W_i}{\sigma_i}\right)^2\right\}\right), \tag{4}$$

where W_i is the observed $W_r(2796)$ for galaxy i, $\bar{W}$ is the model expectation, and σ_i is the measurement error of W_i. Specifically, the first term takes into account the intrinsic scatter ($\sigma_{\rm insc}$) of a given model expectation ($\bar{W}$) due to variations between individual galaxies and between different sightlines probing the same galaxy (e.g. Chen et al. 2014). Motivated by Fig. 4 and previous studies (e.g. C10), we model the intrinsic scatter as a constant in logarithmic space, independent of galaxy properties, and projected distance. The second term represents the pdf of a normal distribution induced by measurement uncertainty σ_i.

On the other hand, h_i is defined simply as a normal distribution with measurement error σ_i and a mean consistent with absence of gas (i.e. zero)

$$h_i = \frac{1}{\sigma_i\sqrt{2\pi}} \exp\left(-\frac{1}{2}\left[\frac{W_i - 0.0}{\sigma_i}\right]^2\right). \tag{5}$$

We note that for each non-detection, we also measure the rest-frame equivalent width by direct summation of the continuum normalized spectrum over a resolution element, centering at the systematic redshift of the galaxy. This allows us to appropriately exploit the constraints from both detections and non-detections the same way. We multiply the likelihood function of each galaxy i over a total of n target galaxies to obtain the total likelihood function in equation (3). We assess the confidence intervals of derived model parameters using the Markov chain Monte Carlo (MCMC) method.

4.2 Dependence of extended gas on galaxy projected distance

First, we seek the best-fitting models to describe the dependence of $W_r(2796)$ on d (see the upper left panel of Fig. 5; Model I). The maximum likelihood solution for isolated galaxies is

$$\log\ \bar{W}_r(2796) = (0.83 \pm 0.38) - (0.72 \pm 0.25) \log\ d \tag{6}$$

with an intrinsic scatter $\sigma = 0.32 \pm 0.04$ in common logarithm. Note that σ is a simple conversion of $\sigma_{\rm insc}$ (see equation 4) from natural to common logarithm. The errors in the coefficients are 1σ uncertainties. The non-parametric covering fractions are $\epsilon_1 = 0.87 \pm 0.05$, $\epsilon_2 = 0.49 \pm 0.06$, $\epsilon_3 = 0.19 \pm 0.12$, and $\epsilon_4 = 0.06 \pm 0.06$. The intervals of the covering fraction bins are listed in Table 4. The maximum likelihood solution shows a significant anticorrelation ($\sim 3\sigma$ level) between the Mg II absorption strength and projected distance d. Our results also show that the mean gas covering fraction declines steeply as the projected distance increases. We note that the inferred low covering fraction at $d \gtrsim 100$ kpc may be driven by weak absorbers [i.e. $W_r(2796) \lesssim 0.04$ Å] for which our data have insufficient S/N to uncover.

To understand the influence of galaxy types on their Mg II absorbing gas properties, we also obtain the best-fitting models for isolated star-forming and quiescent galaxy samples (respectively the upper middle and right panels of Fig. 5). For star-forming galaxies, we find based on the likelihood analysis a best-fitting model

$$\log\ \bar{W}_r(2796) = (0.94 \pm 0.30) - (0.78 \pm 0.20) \log\ d \tag{7}$$

with an intrinsic scatter $\sigma = 0.28 \pm 0.03$ and mean covering fractions of $\epsilon_1 = 0.92 \pm 0.05$, $\epsilon_2 = 0.56 \pm 0.09$, $\epsilon_3 = 0.19 \pm 0.12$, and $\epsilon_4 = 0.08 \pm 0.08$. Similar to the full sample, the $W_r(2796)$ and incidence of gas for star-forming galaxies both decrease as increasing projected distance. For quiescent galaxies, however, the dependence of Mg II absorbing gas and projected distance reveals a stark contrast. The best-fitting power-law model from the likelihood analysis yields

$$\log \bar{W}_r(2796) = (-0.17 \pm 0.20) - (0.08 \pm 0.34) \log d \quad (8)$$

with $\sigma = 0.34 \pm 0.06$ and covering fractions of $\epsilon_1 = 0.67 \pm 0.11$, $\epsilon_2 = 0.41 \pm 0.10$, $\epsilon_3 = 0.09 \pm 0.07$, and $\epsilon_4 = 0.04 \pm 0.04$. While the best-fitting mean covering fractions decline with increasing d, they are ~ 30 per cent lower compared to that of the star-forming ones at $d < 300$ kpc. Furthermore, the maximum likelihood solution shows no statistically significant dependence between Mg II absorption strength and d among detections.

In Fig. 2, we show that the star-forming galaxy sample spans a wide range of stellar masses from $M_{\rm star} = 10^8$–$10^{11.3}$, while quiescent galaxies have on average higher stellar masses ranging from $M_{\rm star} = 10^{9.3}$–$10^{11.6}$. It has been shown in observations (e.g. Chen et al. 2010b) and theoretical models (e.g. Mo & Miralda-Escude 1996; Maller & Bullock 2004) that more massive galaxies tend to have more extended gaseous haloes. To address whether the apparent differential observed $\bar{W}_r(2796)$ versus d plane between star-forming and quiescent galaxy samples can be affected by the gaseous haloes with various sizes, we estimate the dark matter halo radius ($R_{\rm h}$) of individual galaxies and examine how Mg II absorption strength varies with $R_{\rm h}$-normalized projected distance ($d/R_{\rm h}$). The halo radius $R_{\rm h}$ is calculated following the prescription in Liang & Chen (2014). Specifically, we obtain halo mass ($M_{\rm h}$) using the stellar-mass-to-halo-mass relation derived in Kravtsov, Vikhlinin & Meshcheryakov (2018), and $M_{\rm h}$ is then converted to $R_{\rm h}$ with standard cosmology (Bryan & Norman 1998).

We present the correlation between $\bar{W}_r(2796)$ and galaxy $R_{\rm h}$-normalized projected distance ($d/R_{\rm h}$) in the lower panels of Fig. 5 (Model II). We note that Mg II absorbing gas declines steeply beyond $0.4\,R_{\rm h}$. Essentially only one galaxy at $d = 0.66\,R_{\rm h}$ has an associated Mg II absorber. The maximum likelihood solution for the full isolated galaxy sample is

$$\log \bar{W}_r(2796) = (-0.88 \pm 0.15) - (0.84 \pm 0.20) \log[d/R_{\rm h}] \quad (9)$$

with an intrinsic scatter $\sigma_c = 0.29 \pm 0.03$ and covering fractions of $\epsilon_1 = 0.85 \pm 0.06$, $\epsilon_2 = 0.57 \pm 0.08$, $\epsilon_3 = 0.10 \pm 0.06$, and $\epsilon_4 = 0.07 \pm 0.07$.

We find that after accounting for the mass scaling of gaseous radius, the slope of the anticorrelation is steepened by 17 per cent and becomes more statistically significant. For the isolated star-forming galaxies, we obtain a similar improvement based on the likelihood analysis

$$\log \bar{W}_r(2796) = (-0.98 \pm 0.17) - (1.03 \pm 0.22) \log[d/R_{\rm h}] \quad (10)$$

with an intrinsic scatter $\sigma_c = 0.26 \pm 0.03$ and covering fractions of $\epsilon_1 = 0.95 \pm 0.04$, $\epsilon_2 = 0.67 \pm 0.08$, $\epsilon_3 = 0.18 \pm 0.10$, and $\epsilon_4 = 0.12 \pm 0.12$. The best-fitting result also shows a steeper slope by 32 per cent and a $\sim 5\sigma$ significance of the anticorrelation. In contrast, including scaling with $R_{\rm h}$ does not improve the observed $\bar{W}_r(2796)$ versus $R_{\rm h}$ anticorrelation for the quiescent galaxy sample. We find a best-fitting model of

$$\log \bar{W}_r(2796) = (-0.48 \pm 0.27) - (0.12 \pm 0.24) \log[d/R_{\rm h}] \quad (11)$$

with an intrinsic scatter $\sigma_c = 0.37 \pm 0.09$ and covering fractions of $\epsilon_1 = 0.53 \pm 0.18$, $\epsilon_2 = 0.39 \pm 0.15$, $\epsilon_3 = 0.07 \pm 0.07$, and $\epsilon_4 = 0.05 \pm 0.05$. The observed Mg II absorption strength versus $d/R_{\rm h}$ remains consistent with a flat distribution.

On the other hand, previous studies have shown that galaxy B-band luminosity, which is a direct observable, also has an impact on both the extent of Mg II absorbing gas and absorption strength (e.g. Chen & Tinker 2008; C10). Therefore, we include rest-frame B-band magnitude $M_{\rm B}$ in the power-law model ($X \equiv M_{\rm B} - M_{\rm B_*}$ in equation 2) to examine how Mg II absorber strength scales with $M_{\rm B}$ (Model III). We adopt $M_{\rm B_*} = -20.6$ from Faber et al. (2007), the characteristic B-band magnitude for describing blue galaxy population at $z \sim 0.4$. Based on the maximum likelihood analysis, we find the Mg II gaseous extent scales with d and $M_{\rm B}$ following

$$\log \bar{W}_r(2796) = (1.22 \pm 0.25) - (0.94 \pm 0.16) \log d - (0.09 \pm 0.03) \times (M_{\rm B} - M_{\rm B*}) \quad (12)$$

with an intrinsic scatter of $\sigma_c = 0.28 \pm 0.03$ and covering fractions of $\epsilon_1 = 0.95 \pm 0.04$, $\epsilon_2 = 0.58 \pm 0.09$, $\epsilon_3 = 0.11 \pm 0.07$, and $\epsilon_4 = 0.04 \pm 0.04$. The results show that including the intrinsic B-band luminosity also leads to a steeper slope of the anticorrelation between $W_r(2796)$ and d. Note that $M_{\rm B}$ has a negative correlation coefficient, consistent with the expectation that brighter galaxies have larger extent of gas.

For star-forming galaxies, we also perform the likelihood analysis and find the observed absorber strength is best described by

$$\log \bar{W}_r(2796) = (1.57 \pm 0.28) - (1.14 \pm 0.18) \log d - (0.12 \pm 0.02) \times (M_{\rm B} - M_{\rm B*}) \quad (13)$$

with an intrinsic scatter $\sigma_c = 0.25 \pm 0.03$ and covering fractions of $\epsilon_1 = 0.97 \pm 0.02$, $\epsilon_2 = 0.60 \pm 0.08$, $\epsilon_3 = 0.18 \pm 0.11$, and $\epsilon_4 = 0.05 \pm 0.05$. The results show trends similar to the full isolated galaxy sample. We find a steeper anticorrelation between $W_r(2796)$ versus d and an anticorrelation between absorption strength and $M_{\rm B}$. The intrinsic scatter is slightly smaller than the results obtained without the scaling of B-band luminosity.

For quiescent galaxies, we obtain a best-fitting model of

$$\log \bar{W}_r(2796) = (0.09 \pm 0.33) - (0.27 \pm 0.20) \log d - (0.02 \pm 0.05) \times (M_{\rm B} - M_{\rm B*}) \quad (14)$$

with an intrinsic scatter $\sigma_c = 0.34 \pm 0.06$ and covering fractions of $\epsilon_1 = 0.54 \pm 0.17$, $\epsilon_2 = 0.37 \pm 0.17$, $\epsilon_3 = 0.07 \pm 0.07$, and $\epsilon_4 = 0.03 \pm 0.03$. Contrary to the star-forming galaxies, we do not find strong correlation between $W_r(2796)$ and d. A slight negative correlation between $W_r(2796)$ and $M_{\rm B}$ is shown. The addition of $M_{\rm B}$ scaling in the power-law model does not seem to reduce the intrinsic scatter of the $W_r(2796)$ versus d relation.

It is notable that although $M_{\rm B}$ is known to scale with halo mass (e.g. Zheng, Coil & Zehavi 2007), it also correlates with [O II] luminosity (e.g. Zhu et al. 2009) and thus might be coupled with recent star-formation. Here, we inspect the correlation between $W_r(2796)$ and total stellar mass $M_{\rm star}$, which is believed to be a good tracer of halo mass (More et al. 2011; Model IV).

We obtain the best-fitting models with the scaling of total stellar mass $M_{\rm star}$ of

$$\log \bar{W}_r(2796) = (1.35 \pm 0.25) - (1.05 \pm 0.17) \log d + (0.21 \pm 0.08) \times (M_{\rm star} - M_{\rm star*}) \quad (15)$$

where $\log M_{\rm star*}/{\rm M}_\odot = 10.3$. The best-fitting intrinsic scatter is $\sigma_c = 0.28 \pm 0.03$ and best-fitting covering fractions are $\epsilon_1 = 0.85 \pm 0.06$, $\epsilon_2 = 0.53 \pm 0.07$, $\epsilon_3 = 0.10 \pm 0.07$, and $\epsilon_4 = 0.07 \pm 0.07$. The best-fitting coefficients show a positive correlation between $W_r(2796)$ and

$M_{\rm star}$, and an anticorrelation between $W_r(2796)$ and d, consistent with the results accounting for $M_{\rm B}$.

Next, based on the likelihood analysis the star-forming galaxy sample has a best-fitting model of

$$\log \bar{W}_r(2796) = (1.42 \pm 0.25) - (1.05 \pm 0.17) \log d + (0.21 \pm 0.08) \times (M_{\rm star} - M_{\rm star*}) \quad (16)$$

with an intrinsic scatter $\sigma_c = 0.27 \pm 0.02$ and covering fractions of $\epsilon_1 = 0.97 \pm 0.03$, $\epsilon_2 = 0.64 \pm 0.08$, $\epsilon_3 = 0.17 \pm 0.09$, and $\epsilon_4 = 0.02 \pm 0.02$.

For quiescent galaxies, the best-fitting model with the scaling of stellar mass is

$$\log \bar{W}_r(2796) = (0.01 \pm 0.36) - (0.24 \pm 0.21) \log d + (0.01 \pm 0.03) \times (M_{\rm star} - M_{\rm star*}) \quad (17)$$

with an intrinsic scatter $\sigma_c = 0.38 \pm 0.04$ and covering fractions of $\epsilon_1 = 0.50 \pm 0.16$, $\epsilon_2 = 0.26 \pm 0.12$, $\epsilon_3 = 0.08 \pm 0.06$, and $\epsilon_4 = 0.09 \pm 0.09$. The results of the likelihood analyses are summarized in Table 4.

Finally, to assess the significance of the anticorrelation without model dependence, we also perform a non-parametric, generalized Kendall's τ test (Feigelson & Nelson 1985) that accounts for the presence of non-detections. The results of Kendall's τ test are presented in Table 4. We find that the $W_r(2796)$ versus d for isolated galaxies deviate from a random distribution at more than an 11σ level. The $W_r(2796)$ is anticorrelated with d at $>10\sigma$ level of significance for isolated, star-forming galaxies. The distribution of $W_r(2796)$ versus d after accounting for $R_{\rm h}$, $L_{\rm B}$, or $M_{\rm star}$ shows similar level of significance. For isolated, quiescent galaxy sample, the significance of the generalized Kendall test is at $\sim 4\sigma$ level, weaker than the significance for star-forming galaxy sample. In our likelihood analysis, we treat an upper limit as either the QSO sightline intercepts Mg II gas but below the detection limit or simply does not intercept Mg II gas. The generalized Kendall test considers all data to follow a single distribution and therefore sensitive upper limits contribute significantly to the anticorrelation in the generalized Kendall test compared to the likelihood analysis.

5 DISCUSSION

We have established a spectroscopic sample of 211 isolated galaxies and 43 non-isolated galaxies with constraints on Mg II absorption from background quasars at projected distances of $d < 500$ kpc. We characterized the cool gas contents of galaxy host haloes as a function of projected distance. We performed likelihood analysis for the isolated galaxies to study the dependence of Mg II gas on galaxy projected distance d. Here, we present the observed mean covering fraction (κ) of Mg II absorbing gas and examine how the incidence of cool gas varies with galaxy properties (i.e. B-band magnitude, stellar mass, and H α equivalent width). We discuss the kinematics, physical conditions, and azimuthal dependence of these Mg II absorbers. Finally, we discuss the properties of gaseous haloes around different host galaxies and compare our results with previous studies.

5.1 Covering fraction of Mg II absorbers

In the previous section, we show that while Mg II absorption equivalent widths of individual absorbers decrease with increasing distance for star-forming galaxies, no clear trends are seen for quiescent galaxies. On the other hand, the best-fitting results of the likelihood analysis suggest a strong anticorrelation between covering fraction of Mg II gas (ϵ) and projected distance for both samples (Table 4). Take model I for example, the best-fitting Mg II gas covering fraction for star-forming galaxies at $d < 40$ kpc is $\epsilon_1 = 0.87 \pm 0.05$, which declines to $\epsilon_2 = 0.49 \pm 0.06$ at $d = 40$–100 kpc. For quiescent galaxies, the covering fraction is $\epsilon_1 = 0.67 \pm 0.11$ at $d < 40$ kpc, which subsequently declines to $\epsilon_2 = 0.41 \pm 0.10$ at $d = 40$–100 kpc. Beyond $d = 100$ kpc, both samples show covering fraction consistent with $\epsilon \approx 0$ within 2σ level. Similar anticorrelations are also reported in the best-fitting results of Model II–Model IV, regardless of various scaling relations with halo radius, B-band magnitude and stellar mass.

We note that the Mg II covering fraction (ϵ) derived using the likelihood analysis denotes the *intrinsic* incidence of Mg II gas, which does not depend on the absorption strength of Mg II. In practice, given the sensitivity of the background QSO spectra, our survey does not provide much information for Mg II absorbers weaker than 0.1 Å. Here, we also report the observed mean covering fraction (κ) of Mg II absorbing gas and examine how the incidence of cool gas varies with galaxy properties. Following the prescription in C10, we employ a maximum likelihood analysis to estimate κ and its uncertainties. The likelihood of detecting an ensemble of galaxies of which n galaxies with associated Mg II absorbers of $W_r \geq W_0$ and m galaxies with no absorbers detected down to a sensitive limit of $W_r < W_0$ is

$$\mathscr{L}(\kappa | W_0) = \langle \kappa \rangle^n \, [1 - \langle \kappa \rangle]^m. \quad (18)$$

We evaluate κ for a detection threshold of $W_0 = 0.3$ Å. In the isolated galaxy samples, 201/211 MagE spectra of corresponding QSOs have sufficient S/N for detecting Mg II gas with absorption strength exceeding $W_r(2796) \geq 0.3$ Å. We evenly divide each sample into various projected distance intervals, and obtain best-fitting observed covering fractions (κ) and associated uncertainties for each projected distance bin. The results are shown in the left-hand panel of Fig. 7.

For the star-forming galaxy sample, the covering fraction of $W_r(2796) \geq 0.3$ Å absorbers declines from $\langle \kappa \rangle = 0.83^{+0.06}_{-0.05}$ at $d < 40$ kpc to $\langle \kappa \rangle = 0.37^{+0.07}_{-0.07}$ at $d \approx 40$–90 kpc. Beyond $d \approx 100$ kpc, the covering fraction declines to $<\kappa> \approx 0$. Quiescent galaxies exhibit similar but mildly lower observed Mg II covering fraction at inner projected distances (< 90 kpc). At $d < 40$ kpc, $\langle \kappa \rangle = 0.57^{+0.16}_{-0.18}$ for quiescent galaxies, which decreases to $\langle \kappa \rangle = 0.28^{+0.11}_{-0.09}$ at $d \approx 40$–90 kpc and subsequently to $\langle \kappa \rangle = 0.02^{+0.03}_{-0.01}$ beyond $d \approx 100$ kpc. The observed anticorrelations between covering fraction and projected distance for both samples are consistent with the best-fitting results from the likelihood analysis. We find that star-forming galaxies seem to have elevated incidence of Mg II gas at inner projected distance of $d < 40$ kpc compared to our quiescent galaxy sample.

To take into account the possible correlation between covering fraction and galaxy properties, we also calculate the mean observed covering fractions in different $M_{\rm B}$-normalized projected distance intervals, using the best-fitting scaling relation of equation (16). The results are shown in the right-hand panel of Fig. 7. After applying the $M_{\rm B}$-scaling, the anticorrelation between covering fraction and normalized projected distance for star-forming galaxies is strengthened. The Mg II gas covering fraction for star-forming galaxies is $\langle \kappa \rangle = 0.93^{+0.03}_{-0.04}$ at $d' < 40$ kpc and $\langle \kappa \rangle = 0.36^{+0.07}_{-0.07}$ at $d' = 40$–100 kpc, where $d' = d \times 10^{0.10(M_{\rm B} - M^*_{\rm B})}$ is the $M_{\rm B}$-normalized projected distance. For quiescent galaxies, we obtain $\langle \kappa \rangle = 0.55^{+0.14}_{-0.15}$ at $d' < 40$ kpc and $\langle \kappa \rangle = 0.2^{+0.12}_{-0.08}$ at $d' = 40$–100 kpc. At inner $d' \lesssim 40$ kpc, the incidence of Mg II gas seems to be suppressed in the quiescent galaxy sample compared to that of star-forming galaxies at $\sim 3\sigma$ level. The fact that the difference in covering fraction between the two samples is more evident after the $M_{\rm B}$-scaling highlights that

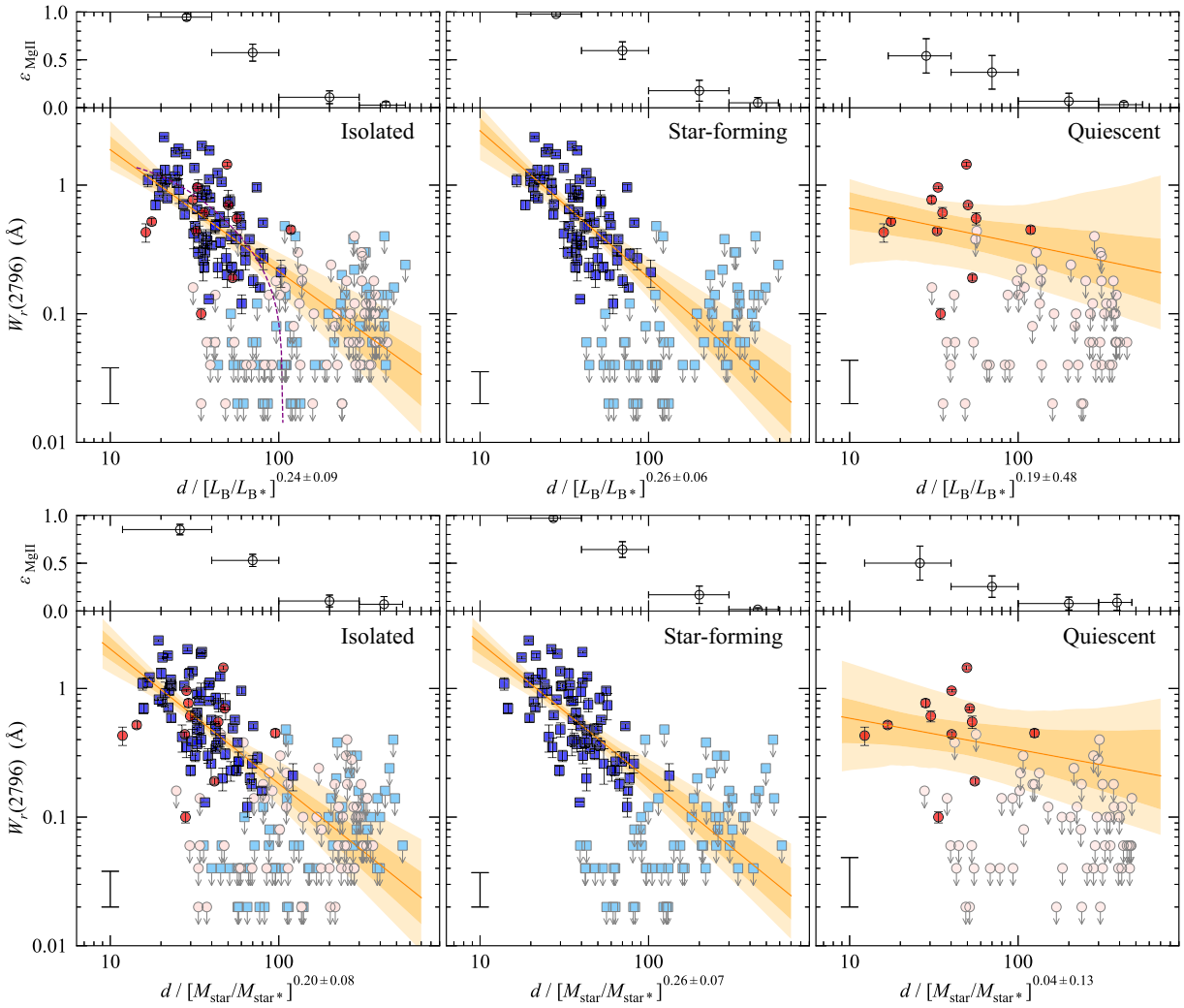

Figure 6. Similar to Fig. 5, but the correlation between $W_r(2796)$ versus d also accounts for the scaling with galaxy B-band luminosity in the upper panels and stellar mass in the lower panels. Note that the scaling coefficients $a' \equiv 2.5 \times (a_2/a_1)$ in $d' = d/[L_{\rm B}/L_{\rm B*}]^{a'}$ and $a'' \equiv -(a_2/a_1)$ in $d' = d/[M_{\rm star}/M_{\rm star*}]^{a''}$ are calculated based on the best-fitting models in equations (12)–(17). For comparison, the purple dashed curve in the upper left panel represents the best-fitting isothermal model from C10.

there is an unambiguous connection between the Mg II gas and host galaxy properties.

Indeed, the high Mg II gas covering fractions of both star-forming and quiescent galaxy samples at $d < 90$ kpc are in stark contrast to what we have seen in luminous red galaxies (LRGs; Huang et al. 2016), which we also show in the left-hand panel of Fig. 7 for comparison. In Huang et al. (2016), we utilized ∼38 000 LRG–QSO pairs in SDSS DR12 and divided the LRGs into passive (purple diamonds) and LINER-like subsamples (green triangles) according to whether they exhibit [O II]-emission features. We reported a constant Mg II gas covering fraction of merely ≈ 15 per cent at $d \lesssim 120$ kpc for passive LRGs, which comprises the majority of the LRG sample (∼ 90 per cent). The LINER-like LRGs have a slightly elevated covering fraction of ≈ 40 per cent at $d < 40$ kpc, which declines to a similar level of ≈ 15 per cent at $d \approx 100$ kpc. We also display the measurement of quasar host haloes from Johnson et al. (2015b) for comparison. The luminous quasars of bolometric luminosity $\log L_{\rm bol}/({\rm erg\,s^{-1}}) > 45.5$ at $\langle z \rangle \approx 1$ are shown in light blue pentagons and low-luminosity ones of $\log L_{\rm bol}/({\rm erg\,s^{-1}}) < 45.5$ at $\langle z \rangle \approx 0.75$ are shown in magenta stars. Both the luminous and low-luminosity quasars exhibit substantial amount of Mg II absorbing gas ($\kappa \approx 0.42$ and $\kappa \approx 0.13$, respectively) at $d = 100$–200 kpc, and elevated Mg II covering fraction of $\kappa \approx 0.9$ and $\kappa \approx 0.5$ within 100 kpc compared to our isolated star-forming and quiescent galaxy samples.

We note that LRGs are luminous and massive ($M_{\rm star} \sim 10^{11.4}$ M$_\odot$), residing in haloes of $M_{\rm halo} \gtrsim 10^{13}$ M$_\odot$ (e.g. Zhu et al. 2014; Huang et al. 2016). The galaxies in our samples are primarily fainter, spanning a broad range of stellar mass from $10^{8.6}$–$10^{11.5}$, with a median stellar mass $M_{\rm star} = 10^{10.5}$. Using our large galaxy samples with sensitive limits of Mg II absorption, we can examine how the observed mean Mg II covering fraction depends on the stellar mass. To perform a representative comparison across a broad range of stellar mass, the mean covering fraction is calculated based on observations of Mg II absorbing gas within a fiducial halo gas radius, $R_{\rm gas}$ (Kacprzak et al. 2008; C10). In C10, we used a sample of 71 isolated galaxies from this survey to show that the extent of Mg II absorbing haloes is well described by an isothermal density profile with a boundary at $d = R_{\rm gas}$, that scales with galaxy B-band luminosity according to $R_{\rm gas} \approx 107 \times (L_B/L_B^*)^{0.35}$ kpc. We equally

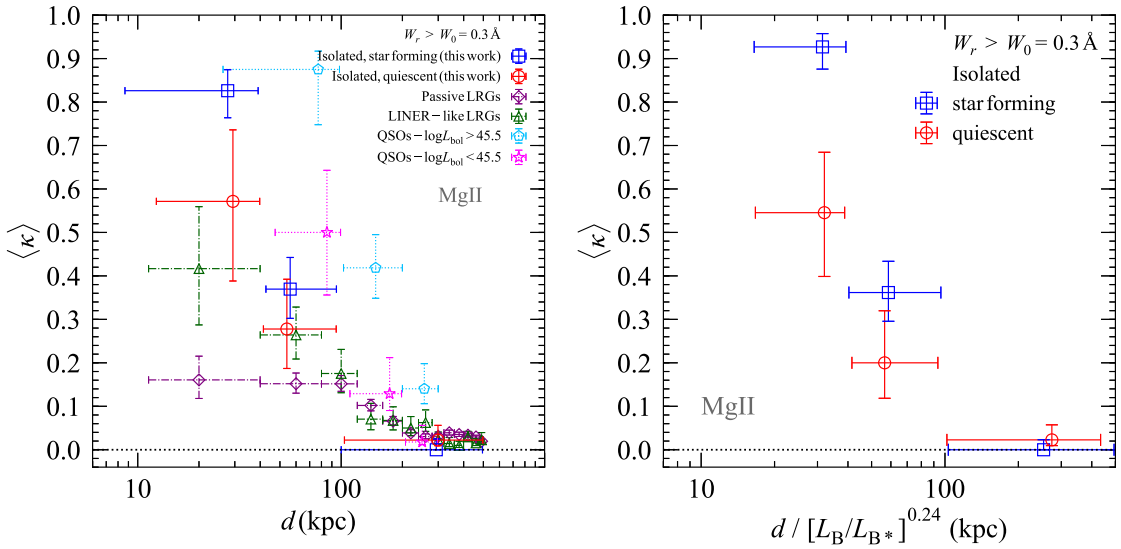

Figure 7. Mean covering fraction of Mg II absorbers $\langle\kappa\rangle$ versus projected distance d (left-hand panel) and versus d accounting for the galaxy B-band luminosity scaling relation (right-hand panel). We show the gas covering fraction of isolated, star-forming galaxies as blue solid squares, and that of isolated, quiescent galaxies as red solid circles. For comparison, we also include covering fraction measurements from the SDSS LINER-like and passive LRG samples of Huang et al. (2016) in green dash–dotted triangles and purple dash–dotted diamonds, respectively. We also show the covering fraction for luminous quasars ($\log L_{\rm bol}/{\rm erg\,s^{-1}} > 45.5$) in light blue dotted pentagons and low-luminosity quasars ($\log L_{\rm bol}/{\rm erg\,s^{-1}} < 45.5$) in magenta dotted stars (Johnson et al. 2015b). The gas covering fraction is computed for a detection threshold of $W_0 = 0.3$ Å. Error bars represent the 68 per cent confidence interval.

divide our star-forming galaxies into two mass intervals, with median stellar masses of $10^{9.7}$ and $10^{10.5}\,{\rm M}_\odot$. The corresponding $R_{\rm gas}$ is respectively around 70 kpc and 100 kpc. For LRGs with a mean luminosity of $\approx 3.6L_*$, we infer $R_{\rm gas} \approx 206$ kpc.

We present in the left-hand panel of Fig. 8 the mean gas covering fraction $\langle\kappa\rangle$ within $R_{\rm gas}$ for our star-forming and quiescent galaxy samples, and the LRG samples in Huang et al. (2016). We show $\langle\kappa\rangle$ for absorption equivalent width thresholds $W_0 = 0.3$ Å (solid symbols) and $W_0 = 0.1$ Å (open symbols). A number of interesting features are revealed in this plot.

At the $W_0 = 0.3$ Å threshold, first the star-forming galaxies display a slightly elevated gas covering fraction from $\langle\kappa\rangle = 0.56^{+0.07}_{-0.08}$ at $M_{\rm star} \approx 10^{9.7}\,{\rm M}_\odot$ to $\langle\kappa\rangle = 0.70^{+0.06}_{-0.07}$ at $M_{\rm star} \approx 10^{10.5}\,{\rm M}_\odot$. Secondly, there is an apparent difference in covering fraction between the star-forming and quiescent galaxy samples for L_* galaxies. The covering fraction for quiescent galaxies is $\langle\kappa\rangle = 0.30^{+0.10}_{-0.09}$ at $M_{\rm star} \approx 10^{10.8}\,M_\odot$, merely ≈ 40 per cent of what we observe in star-forming galaxy haloes. Finally, a sharp decline of Mg II gas covering fraction is revealed from even quiescent L_* galaxies to massive LRGs. Specifically, $\langle\kappa\rangle$ declines from 30–70 per cent around L_* galaxies to $\approx$ 10–15 per cent around massive LRGs. The strong mass dependence of Mg II covering fraction qualitatively agrees with the expectation from the observed clustering of Mg II absorbers, where the Mg II covering fraction peaks at $M_{\rm halo} \sim 10^{12}\,{\rm M}_\odot$ ($\sim L_*$ galaxies) and rapidly falls off at smaller and higher masses (Tinker & Chen 2008, 2010).

In the right-hand panel of Fig. 8, we present the mean gas covering fraction $\langle\kappa\rangle$ within $R_{\rm gas}$ as a function of H α equivalent width for our MagE galaxies and the LRG samples in Huang et al. (2016). The symbols are the same as in the left-hand panel. We find that there is a positive correlation between $\langle\kappa\rangle$ and H α equivalent width (or star formation rate). We note that although LINER-like LRGs (green triangles) have significantly lower $\langle\kappa\rangle$ compared to the MagE quiescent galaxy sample, in Huang et al. (2016) we find that their H α is likely contributed by post-asymptotic giant branch (post-AGB) stars. Therefore, the star formation rates of LRG samples represent upper limits.

5.2 Kinematics

The line-of-sight velocity dispersion of Mg II absorbers provides important insights into the underlying motion and physical nature of cool clumps within host haloes. The left-hand panel of Fig. 9 displays the relative velocity between Mg II absorbers and their host galaxies as a function of inferred dark matter halo mass. The dashed curves mark the projected escape velocities at $r = 30$, 60, 90 kpc (from outside to inside) with respect to mass. No significant trends are observed between the relative velocity and the projected distance between QSO–galaxy pairs. Below projected distance $d < 40$ kpc, we find the median relative velocity difference to be $\langle|\Delta v|\rangle = 48$ km s^{-1}. At $d \geq 40$ kpc, the relative velocity difference is $\langle|\Delta v|\rangle = 47$ km s^{-1}. At similar stellar masses, quiescent galaxies seem to have higher relative velocity offsets from the galaxy systematic redshifts compared to that of star-forming galaxies. The majority of the detected Mg II absorbing gas is found at velocities below the expected projected escape velocities, indicating that these Mg II gas complexes are likely to be gravitationally bound.

Using the large sample of galaxy and absorber pairs in the M3 Halo Project, we are able to constrain how the ensemble average of the velocity distribution of absorbing gas changes with their host galaxy properties. We divide isolated galaxy sample into low-mass ($\log\langle M_{\rm star}/{\rm M}_\odot\rangle \approx 9.7$) and high-mass ($\log\langle M_{\rm star}/{\rm M}_\odot\rangle \approx 10.6$) galaxies to investigate the correlation between mass and velocity dispersion in the middle panels of Fig. 9. The velocity distribution is well characterized by a Gaussian of dispersion $\sigma = 69$ km s^{-1} around low-mass galaxies and $\sigma = 117$ km s^{-1} for high-mass galaxies. Quiescent galaxies seem to have higher relative velocities than that of star-forming galaxies. If we consider only star-forming galaxies, we find that the relative velocity dispersion of low-mass galaxies is $\sigma = 67$ km s^{-1}, and is $\sigma = 83$ km s^{-1} for high-mass galaxies. The

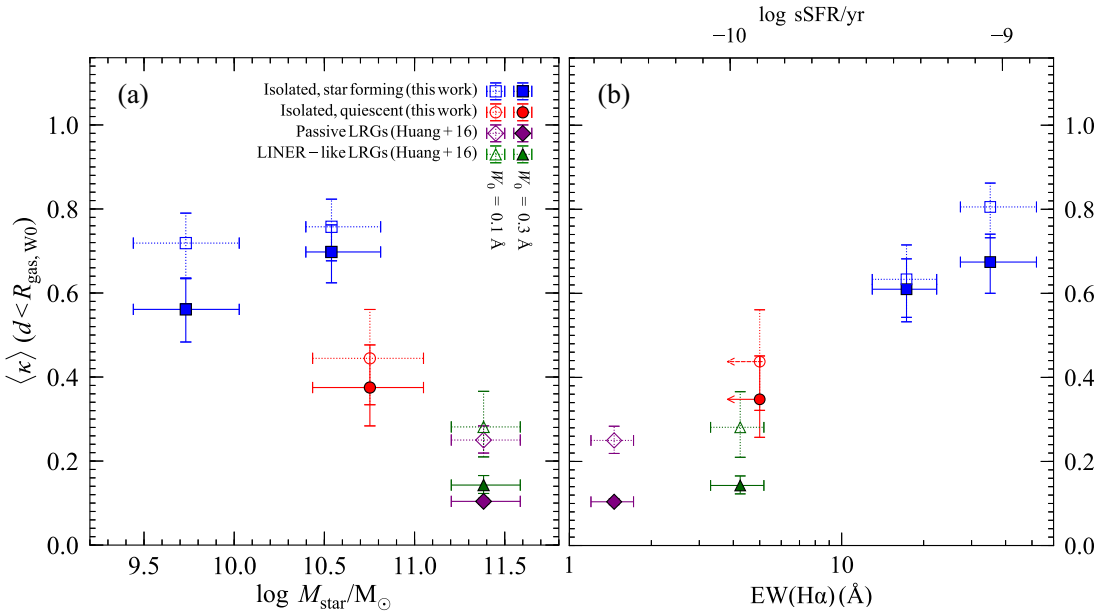

Figure 8. (a) Mass dependence of the mean covering fraction of Mg II absorbing gas. Isolated, star-forming galaxies are shown in blue squares, and quiescent galaxies are shown in red circles. Constraints from passive LRGs and [O II]-emitting LRGs are included as purple diamonds and green triangles (Huang et al. 2016). Solid points indicate absorbers of $W_0 = 0.3$ Å, and open points indicate absorbers of $W_0 = 0.1$ Å. The horizontal bars represent 68 per cent range of stellar mass for galaxies included in each bin, and the vertical error bars show the 68 per cent confidence interval. (b) H α equivalent width versus the mean covering fraction of Mg II absorbing gas. The symbols are the same as (a). The inferred specific star-formation rate (sSFR) on the top axis is derived from Section 3.1. Note that the H α emission for some passive galaxies is likely due to the underlying AGNs or LINERs, and therefore the inferred sSFR based on the observed H α emission only represents an upper limit.

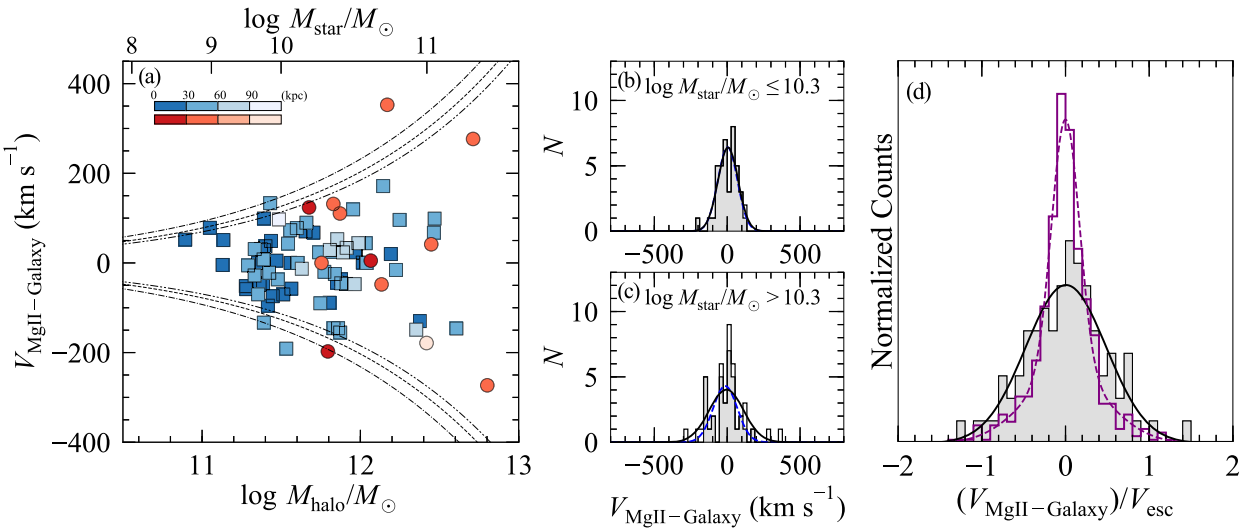

Figure 9. Left: Relative Mg II absorption velocities with respect to the galaxy systematic redshifts as a function of inferred dark matter halo mass for isolated, star-forming (blue squares) and quiescent (red circles) galaxies. The darkness of the blue/red symbols indicates galaxies at various projected distances according to the colour bars in the top left corner. The three pairs of dashed curves from outside to inside mark the line-of-sight projected halo escape velocities at distance $r = 30$, 60, and 90 kpc, assuming an NFW profile of dark matter haloes. Middle: The relative velocity distributions of Mg II absorbers for low-mass ($M_{\rm star} \le 10^{10.3}$ M$_\odot$; top middle panel) and high-mass ($M_{\rm star} > 10^{10.3}$ M$_\odot$; bottom middle panel) galaxies. The filled and open histograms represent respectively the number counts for isolated full and star-forming galaxy samples. Adopting a Gaussian profile to characterize the velocity distribution of Mg II gas around low-mass (high-mass) galaxies leads to a Gaussian profile centred at $\langle v_{\rm Mg\,II\text{-}Galaxy}\rangle = 6(-5)$ km s^{-1} and $\sigma = 69$ (117) km s^{-1} (black solid curves). Considering only star-forming galaxies for the low-mass (high-mass) galaxy sample, we find a mean and dispersion of $\langle v_{\rm Mg\,II\text{-}Galaxy}\rangle = 3(-13)$ km s^{-1} and $\sigma = 67$ (83) km s^{-1} (blue dashed curves). Right: The relative velocity distributions of Mg II absorbers normalized by the line-of-sight projected halo escape velocities ($V_{\rm esc}$) at the projected distance for isolated galaxies (filled histogram; this work) and passive LRGs (purple open histogram; Huang et al. 2016). Mg II-absorbing gas around isolated galaxies can be characterized by a single Gaussian distribution centred at $\langle v_{\rm Mg\,II\text{-}Galaxy}\rangle/v_{\rm esc} = 0.01$ and $\sigma = 0.48$ (black curve). Applying a double Gaussian profile similar to Huang et al. (2016), Mg II-absorbing gas around passive LRGs can be characterized by a narrow component centred at $\langle v_{\rm Mg\,II\text{-}Galaxy}\rangle/v_{\rm esc} = 0.00$ and $\sigma = 0.17$ and a broad component centred at $\langle v_{\rm Mg\,II\text{-}Galaxy}\rangle/v_{\rm esc} = 0.00$ and $\sigma = 0.50$ (purple dashed curve).

velocity dispersion of the high-mass sample is ≈ 20 per cent more elevated than the low-mass sample.

We use the bootstrap method to estimate the 68 per cent confidence levels of the relative velocity dispersion. For isolated star-forming galaxies, the low-mass sample gives $\sigma = 58$–$73\,\mathrm{km\,s^{-1}}$, while the high-mass sample gives $\sigma = 73$–$90\,\mathrm{km\,s^{-1}}$. There seems to be a positive correlation between the velocity dispersion of Mg II absorbing gas and mass of associated host haloes. Assuming a Navarro–Frenk–White (NFW) profile (Navarro, Frenk & White 1997) with halo concentration of $c_\mathrm{h} = 10$, we can calculate the expected line-of-sight velocity dispersion for virialized motion within $d = 100\,\mathrm{kpc}$, beyond which no Mg II gas is detected in the isolated star-forming galaxy sample. The expected line-of-sight velocity dispersion for low-mass and high-mass galaxies are respectively $\sigma = 52\,\mathrm{km\,s^{-1}}$ and $\sigma = 86\,\mathrm{km\,s^{-1}}$, comparable to the observed velocity dispersion. The recent work on Mg II absorbing gas around 50 star-forming galaxies at $z \approx 0.2$ (Martin et al. 2019) also shows a consistent result. With a median stellar mass of $M_\mathrm{star} = 10^{10}\,\mathrm{M_\odot}$, the sample has a relative velocity dispersion of $\sigma = 42$–$54\,\mathrm{km\,s^{-1}}$, comparable to the expected line-of-sight velocity dispersion of $\sigma = 56\,\mathrm{km\,s^{-1}}$.

Our result is in stark contrast to the Mg II gas in LRG haloes, where the line-of-sight velocity dispersion is merely 60 per cent of what is expected from virial motion (Zhu et al. 2014; Huang et al. 2016; Afruni, Fraternali & Pezzulli 2019; Zahedy et al. 2019). In the right-hand panel of Fig. 9, we display the relative velocity distributions of Mg II absorbers divided by the line-of-sight projected halo escape velocity for our isolated galaxies (filled histogram) and passive LRGs in Huang et al. (2016, open histogram). It is clear that while for both samples the majority of the detected Mg II absorbing gas is at velocities well within the expected projected escape velocities, Mg II gas found around passive LRGs have suppressed velocity dispersion compared to our isolated galaxies. Since the Kolmogorov–Smirnov (K–S) test tends to be most sensitive around the median values of distributions and less sensitive to the tails of distributions, we use Anderson–Darling (A–D) test (Anderson & Darling 1952), which provide increased sensitivity on the shapes of distributions. The A–D test shows that the probability of the two velocity dispersions of Mg II absorbers to be drawn from the same distribution is $P \sim 1.4$ per cent.

The comparable velocities between observation and the expectation from virial motion support the physical formalism for a two-phase CGM, where QSO absorption systems in the vicinity of galaxies originate in cool clumps that are in thermal pressure equilibrium with the hot halo (Mo & Miralda-Escude 1996). The positive correlation between the mean gas covering fraction $\langle\kappa\rangle$ and H α equivalent width (sSFR) in the right-hand panel of Fig. 8 also hints on the possibility that the cool clumps may be able to survive and reach the central galaxy.

If clouds are sufficiently massive, they can travel at a characteristic speed equal to the halo velocity as the clouds move through host gas halo. Following Maller & Bullock (2004), we are able to place a lower limit on the cloud mass using their equation (40),

$$m_\mathrm{cl} \approx 5.1 \times 10^4\,\mathrm{M_\odot}\,T_6^{-3/8}(\Lambda_z t_8)^{1/2} \tag{19}$$

where $T_6 = T/10^6\,\mathrm{K}$ is the temperature of hot halo gas, Λ_z is a cooling parameter that depends on the gas metallicity, and $t_8 = t_f/8$ Gyr is the halo formation time-scale. For our low-mass and high-mass galaxy samples of $\log\langle M_\mathrm{star}/\mathrm{M_\odot}\rangle \approx 9.7$ and 10.6, $T \sim 5 \times 10^5\,\mathrm{K}$ and $T \sim 10^6\,\mathrm{K}$ assuming an isothermal gas, and $t_f \sim 9$ Gyr according to *N*-body simulations (Wechsler et al. 2002). We find the lower limits of cloud mass are $m_\mathrm{cl} = (0.7, 1.5) \times 10^5\,\mathrm{M_\odot}$ for low-mass galaxies and $m_\mathrm{cl} = (0.5, 1.1) \times 10^5\,\mathrm{M_\odot}$ for high-mass galaxies assuming (0.1, 1.0) solar metallicity. The cloud mass is qualitatively consistent with the initial cloud mass of $\approx 10^{4-5}\,\mathrm{M_\odot}$ at the virial radius in Afruni et al. (2019). Unlike massive LRG haloes, the inflow accretion of gas clouds from external parts of L_* galaxy haloes does not suffer from severe deceleration by the hot gas drag force, and therefore remain massive in the internal regions.

We estimate the free-fall time (τ_ff) for the clouds to reach the centre to be $\tau_\mathrm{ff} \sim 0.29$ Gyr for our Mg II absorbers at projected distance $\langle d\rangle_\mathrm{med} \approx 33$ kpc and $\langle z\rangle_\mathrm{med} \approx 0.23$. This time-scale is about an order of magnitude smaller than the characteristic time-scale for the clouds being evaporated by conduction from the surrounding hot gas. If we assume it takes a free-fall time (τ_ff) for the clouds to reach the centre of the host halo, we can infer a cool gas accretion rate of

$$\dot{M} = 1.33 \left(\frac{f_\mathrm{cl}}{0.1}\right)\left(\frac{m_\mathrm{cl}}{10^5\mathrm{M_\odot}}\right)\left(\frac{r_\mathrm{c}}{1\,\mathrm{kpc}}\right)\,\mathrm{M_\odot\,yr^{-1}}, \tag{20}$$

where f_cl is the volume filling factor of Mg II gas within ≈ 33 kpc, m_cl is the cloud mass, and r_c is the mean clump size. Assuming $f_\mathrm{cl} = 0.1$ and $r_\mathrm{c} = 1$ kpc, we can obtain a lower limit of cool gas accretion rate of $\dot{M} = (0.9, 2.0)\,\mathrm{M_\odot\,yr^{-1}}$ for low-mass galaxies and $\dot{M} = (0.7, 1.5)\,\mathrm{M_\odot\,yr^{-1}}$ for high-mass galaxies assuming (0.1, 1.0) solar metallicity. The estimated accretion rate is similar to the star formation rate of the Milky Way of $\sim 2\,\mathrm{M_\odot\,yr^{-1}}$ (Chomiuk & Povich 2011). Note that given the lower limit of cloud mass we obtain from the equation (19), the characteristic time-scale (τ_evap) for clouds being evaporated by conduction from the surrounding hot gas is about $\tau_\mathrm{evap} \gtrsim 10\tau_\mathrm{ff}$. Therefore, the cool clumps are likely to reach the centre of the host halo.

5.3 Angular distribution of Mg II absorption relative to galaxy major axis

To examine the azimuthal dependence of $<\kappa>$, we calculate the azimuthal angle (Φ) of each galaxy following the same procedure in Huang et al. (2016). Briefly, Φ is calculated using the position angle (PA) and ellipticity (e) measurements from the SDSS data base. The azimuthal angle (Φ) is defined as the angle from the galaxy's major axis to the line connecting the centre of the galaxy to the location of the QSO. A QSO sightline that occurs along the major axis of the galaxy has $\Phi = 0^\circ$ and one that occurs along the minor axis of the galaxy has $\Phi = 90^\circ$.

To ensure a high confidence in the following azimuthal dependence investigation, we restrict our sample to those galaxies with measured ellipticities $e > 0.2$ and consistent measurements of PA in both SDSS r and i bands. SDSS r and i bands are the most sensitive bandpasses for measuring the surface brightness profiles and Φ for galaxies at $z \approx 0.2$ in our sample. A total of 128 out of 201 galaxies meet this criterion. We then divide these galaxies into three bins of Φ, where the bin size is chosen to be larger than the typical uncertainty in our data ($\Delta\Phi < 10^\circ$). In Fig. 10, we display 15 galaxy–QSO pairs to illustrate typical cases with azimuthal angles falling in the three bins: $0^\circ < \Phi \leq 30^\circ$ (top), $30^\circ < \Phi \leq 60^\circ$ (middle), and $60^\circ < \Phi \leq 90^\circ$ (bottom) that go into the calculations in Fig. 11. From visual inspection of Fig. 10, it is clear that the measurements of Φ for the restricted sample are sufficiently adequate for the adopted bin size $\Delta\Phi = 30^\circ$.

We present in the left-hand panel of Fig. 11, the $<\kappa>$ as a function of Φ for our star-forming and quiescent galaxy samples. As we only have one detected Mg II absorber for the isolated galaxy sample beyond $0.4R_\mathrm{h}$, we limit our investigation to $d \leq 0.4\,R_\mathrm{h}$. We find no strong dependence of $<\kappa>$ on Φ for either star-

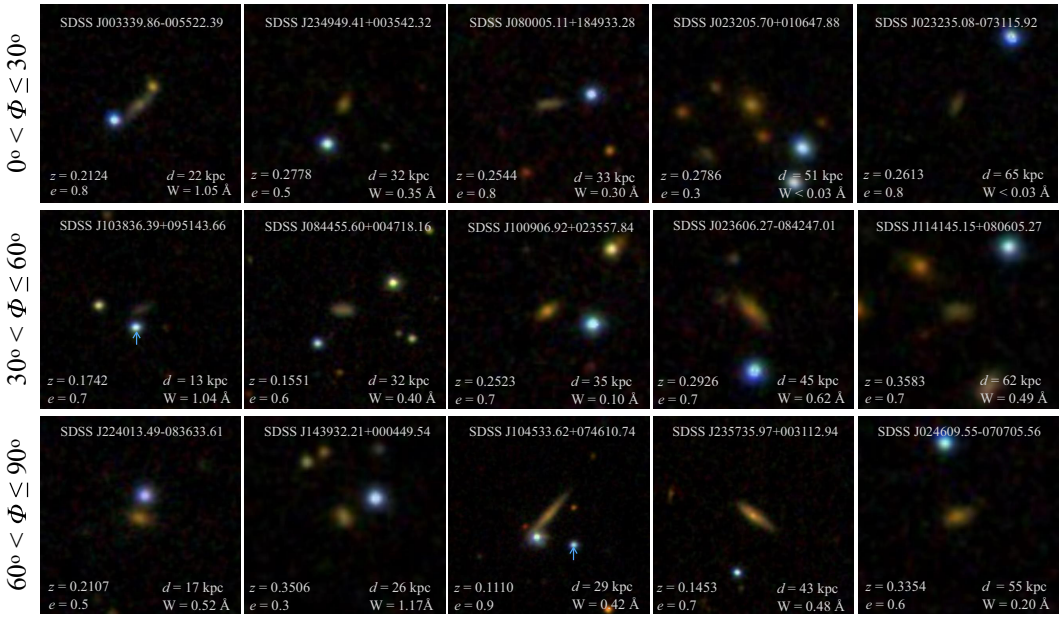

Figure 10. Images of 15 randomly selected galaxy–QSO pairs in our sample to demonstrate that the accuracy of the azimuthal angle (Φ) measurements from SDSS is sufficient for the subsequent Φ-dependence study. Each panel is 150 kpc on a side at the galaxy redshift. Each galaxy is located at the centre and the QSO appears as a blue compact source near the galaxy. We mark QSOs with blue arrows in some panels for clarification. The projected distance (d) and the strength of Mg II absorbers (W; measurement or 2σ upper limits) of each galaxy are shown in the lower-right corner, and the galaxy redshift (z) and the ellipticity (e) are shown in the lower-left corner. The top, middle, and bottom rows show examples of galaxies with azimuthal angle Φ in the range of $0° < \Phi \leq 30°$, $30° < \Phi \leq 60°$, and $60° < \Phi \leq 90°$, respectively. The images in each row are displayed from left to right in increasing projected distance d.

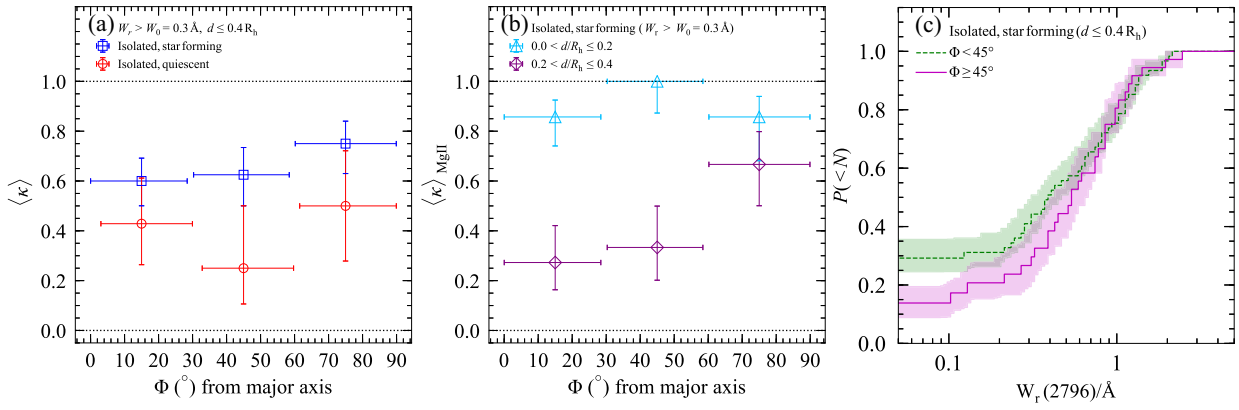

Figure 11. (a) Dependence of $<\kappa>$ on the azimuthal angle for isolated, star-forming galaxies (blue squares) and quiescent galaxies (red circles) at projected distance $d < 0.4\,R_{\rm h}$. (b) Dependence of $<\kappa>$ on the azimuthal angle in different projected distance intervals for isolated, star-forming galaxies. Triangles represent galaxies within projected distance d of $d \leq 0.2\,R_{\rm h}$ from a background QSO sightline, and diamonds represent $0.2\,R_{\rm h} < d \leq 0.4\,R_{\rm h}$ The horizontal error bars show the full range of galaxy–QSO projected distances within each bin and vertical error bars represent the 68 per cent confidence interval. (c) Cumulative fraction (P) of isolated, star-forming galaxies at $d < 0.4\,R_{\rm h}$ with the rest-frame equivalent width of Mg II no greater than $W_r(2796)$/Å. The galaxies with azimuthal angle $\Phi < 45°$ are shown in dashed green line and galaxies with $\Phi \geq 45°$ as magenta solid line. The cumulative distributions are estimated using Kaplan–Meier estimator. The shaded bands represent 68 per cent confidence intervals including uncertainties due to sample variance and $W_r(2796)$ measurement errors with combined bootstrapping and Monte Carlo resampling.

forming or quiescent galaxies. While we find a modest enhancement (≈10 per cent at 1σ level) of Mg II absorption closer to the minor axis ($\Phi \gtrsim 60°$) of star-forming galaxies, no azimuthal angle preference is found for quiescent galaxies. In the middle panel of Fig. 11, we further divide star-forming galaxies into two projected distance bins. We find no azimuthal angle dependence of $<\kappa>$ for star-forming galaxies at small projected distance $0 < d \leq 0.2\,R_{\rm h}$, and a mild elevated covering fraction along the minor axis ($\sim 1\sigma$ level) at $0.2 < d \leq 0.4\,R_{\rm h}$. To further investigate the strength of Mg II absorbers around galaxies closer to the major ($\Phi < 45°$) and minor ($\Phi \geq 45°$) axis, we use the Kaplan–Meier estimator (Feigelson & Nelson 1985) to derive the median rest-frame equivalent width of Mg II and associated error. Based on the Kaplan–Meier curves, we infer a median $W_r(2796) \approx 0.39 \pm 0.08$Å for galaxies with $\Phi < 45°$ and $W_r(2796) \approx 0.53^{+0.13}_{-0.11}$Å for galaxies with $\Phi \geq 45°$. The excess $W_r(2796)$ around galaxies closer to the minor axis ($\Phi \geq 45°$) is at $\lesssim 1\sigma$ level. We find no statistical significant dependence of $<\kappa>$ or $W_r(2796)$ on azimuthal angle Φ.

5.4 Comparison between star-forming and quiescent galaxies

With the large isolated galaxy samples, here we compare the physical properties of Mg II absorbing gas around star-forming and quiescent galaxies. Using our likelihood analysis, we have noted that there is a significant anticorrelation ($\sim 3\sigma$) between the Mg II absorption strength and projected distance d for star-forming galaxies. The anticorrelation becomes even stronger when including scaling with B-band luminosity ($\sim 6\sigma$) and stellar mass ($\sim 8\sigma$). In contrast, the results of likelihood analysis show that the quiescent galaxies do not have a trend in Mg II absorption strength versus projected distance within a $\sim 1\sigma$ level. Including the scaling of B-band luminosity or stellar mass has little improvement on the anticorrelation.

In Fig. 7, we show that both star-forming and quiescent galaxies show steep declining covering fraction $<\kappa>$ with increasing d. For the star-forming galaxy sample, the covering fraction of $W_r(2796) \geq 0.3$ Å absorbers declines from $<\kappa> \approx 0.83$ at $d < 40$ kpc to $<\kappa> \approx 0.37$ at $d \approx 40$–90 kpc (~ 55 per cent decline), similar to that of the quiescent galaxy sample (~ 51 per cent decline). Beyond $d \approx 100$ kpc, the covering fraction of both samples is consistent with $<\kappa> \approx 0$. The dependence of $<\kappa>$ and d for our galaxies is in stark contrast to the massive LRG samples (Huang et al. 2016). Specifically, the passive LRGs display flat distribution of $\langle\kappa\rangle \sim 15$ per cent at $d \lesssim 120$ kpc, and an overall $\langle\kappa\rangle \sim 5$ per cent out to $d \sim 500$ kpc.

Next, in Fig. 8(a) we show that in addition to the strong dependence of covering fraction on galaxy mass, at a similar mass range of $\log M_{\rm star}/{\rm M}_\odot \approx 10.4$–$11.1$, star-forming galaxies reveal an elevated covering fraction than that of quiescent galaxies. Note that despite the higher $<\kappa>$ we obtain for the star-forming galaxies, the sample has on average a slightly lower stellar mass $\log \langle M_{\rm star}/{\rm M}_\odot\rangle$ of ~ 10.5 compared to that of the quiescent galaxy sample ($\log \langle M_{\rm star}/{\rm M}_\odot\rangle \sim 10.7$). To investigate whether the elevated $<\kappa>$ for star-forming galaxies is due to the physical properties of associated galaxies or simply a steep dependence on mass, we restrict the two samples to a narrow stellar mass range of $\log M_{\rm star}/{\rm M}_\odot = 10.4$–$10.7$, making both samples similar stellar mass distributions with $\log \langle M_{\rm star}/{\rm M}_\odot\rangle = 10.55$. We find the resultant covering fraction of star-forming galaxies is 0.64 ± 0.10, while that of quiescent galaxies is 0.29 ± 0.13. With the same stellar mass distribution, the quiescent galaxies have merely 45 per cent gas covering fraction compared to the star-forming galaxies. We find the resultant covering fraction of star-forming galaxies is 0.64 ± 0.10, while that of quiescent galaxies is 0.29 ± 0.13. With the same stellar mass distribution, the quiescent galaxies have merely 45 per cent gas covering fraction compared to the star-forming galaxies. The positive correlation between sSFR and gas covering fraction is manifest in Fig. 8(b). An enhanced Mg II covering fraction around star-forming galaxies seems to imply an outflow origin. However, the origin is complicated by the fact that the majority of Mg II absorbers around isolated galaxies are gravitationally bound (Fig. 9). In addition, no statistically significant dependence of $\langle\kappa\rangle$ or $W_r(2796)$ on the azimuthal angle is found in Section 5.3. Furthermore, the kinematics discussed in Section 5.2 indicates that while cool clumps around star-forming galaxies can reach the centre of the halo, the clumps in massive quiescent haloes are likely to be destroyed during the infall before reaching the LRGs (e.g. Gauthier & Chen 2011; Huang et al. 2016; Zahedy et al. 2019).

5.5 Comparison between isolated and non-isolated systems

In the *right-hand* panel of Fig. 4, we find that the 43 non-isolated systems exhibit no hint of a trend between Mg II absorber strength $W_r(2796)$ and galaxy projected distance d among detections, contrary to the clear anticorrelation shown in isolated galaxies (*central* panel). Specifically, while we do not find any detection beyond ~ 100 kpc for isolated, star-forming galaxies, strong systems of $W_r(2796) \gtrsim 0.5$Å are detected for non-isolated systems at large distances. The results remain unchanged irrespective of whether the distance from nearest galaxy or a luminosity-weighted distance is adopted for non-isolated systems. The result is in line with previous findings that detections of $W_r(2796) \gtrsim 0.5$ Å absorbers are frequently found in non-isolated or group systems at beyond $d \sim 100$ kpc (e.g. C10; Nielsen et al. 2018; Fossati et al. 2019). Indeed, previous studies have discovered strong Mg II absorbers $W_r(2796) > 1$ Å associated with galaxy groups (e.g. Whiting, Webster & Francis 2006; Fossati et al. 2019), LRGs (Gauthier 2013; Huang et al. 2016), and luminous quasar hosts (Johnson et al. 2015a), whereas such absorbers are only found at $d \lesssim 50$ kpc in our 211 isolated galaxy samples.

Recently, new wide-field integral field spectrographs such as the Multi Unit Spectroscopic Explorer (MUSE; Bacon et al. 2010) have enabled discoveries of spatially extended line-emitting nebulae on scales reaching ~ 100 kpc in group or cluster environments (e.g. Epinat et al. 2018; Johnson et al. 2018; Chen et al. 2019). Johnson et al. (2018) found that these giant [O III] nebulae correspond both morphologically and kinematically to interacting galaxy pairs in the group, likely arising from cool filaments and interaction-related debris. Furthermore, covering ~ 20 per cent of the area around the quasar at $\lesssim 100$ kpc, the nebulae may be an explanation of the high covering fraction of Mg II absorbing gas around luminous QSO hosts in Johnson et al. (2015a). Chen et al. (2019) also uncovered a giant nebula (~ 100 physical kpc) associated with a low-mass galaxy group at $z \sim 0.3$, where the line-emitting gas connects between group galaxies and follows closely the motion of member galaxies. The study demonstrates that gas stripping in low-mass groups may be effective in releasing metal-enriched gas from star-forming regions, producing absorption systems (e.g. Mg II absorbers) in QSO spectra.

The case studies of spatially extended line-emitting nebulae associated with galaxy groups provide unambiguous evidence of the importance of interactions in distributing metal-enriched gas on large scales. Despite the lack of morphological information in our absorption-line survey, the commonly found strong Mg II absorbers ($W_r(2796) \gtrsim 0.5$ Å) at $d \gtrsim 100$ kpc in the 43 non-isolated systems support the idea that interactions between group galaxies may contribute to the presence of strong absorbers at large scales.

5.6 Comparison with other studies

The M3 Halo Project consists of 211 isolated and 43 non-isolated galaxies with $z = 0.10$–0.48 at projected distance $\langle d\rangle_{\rm med} = 73$ kpc from a background QSO, chosen without any prior knowledge of the presence or absence of Mg II absorbing gas. The absorption-blind sample chosen from SDSS enables an unbiased characterization of the correlation between Mg II absorbing gas and physical properties of associated galaxies. Our survey shows a distinct difference in the $W_r(2796)$ versus d inverse correlation between star-forming and quiescent haloes. While there is a significant anticorrelation ($\gtrsim 3\sigma$) between $W_r(2796)$ and d for star-forming galaxies, there is no hint of a correlation among Mg II detected quiescent galaxies. We also show that while star-forming galaxies have elevated $\langle\kappa\rangle \approx 83$ per cent at $d < 40$ kpc, both star-forming and quiescent galaxies show $\langle\kappa\rangle \approx 0$ beyond 90 kpc. These findings are dif-

ferent from the results of MAGIICAT (Nielsen et al. 2013a, b). At the $W_0 = 0.3$ Å threshold, MAGIICAT galaxies reveal a non-negligible Mg II gas covering fraction $\langle\kappa\rangle \approx$ 10–40 per cent at $d = 100$–200 kpc.

It is worth noting that even though 69 out of 182 galaxies in MAGIICAT come from our M3 Halo Project (Chen & Tinker 2008; C10), MAGIICAT consists of galaxy–Mg II absorber pairs from different programs. While some of these programs were designed to be absorption-blind like the M3 Halo Project, others select galaxies at the redshifts of known Mg II absorbers. The galaxy–absorber pairs from these other programs have associated Mg II absorbers by design, therefore imposing a strong bias on the calculated gas covering fraction. Similarly, the lack of mass dependence on the covering fraction of Mg II absorbing gas in Churchill et al. (2013) can be understood by an over estimation of covering fraction at high mass, where detections at this mass range come mostly from absorber centric surveys.

Martin et al. (2019) constructed a sample of 50 $z \approx 0.2$ star-forming galaxies with $M_{\rm star} \approx 10^{10}\,{\rm M}_\odot$ at close projected distances $d < 100$ kpc, properties similar to our star-forming galaxies. For absorbers with a detection threshold of $W_0 = 0.3$ Å, this sample yields $\langle\kappa\rangle \approx 75$ per cent at $d < 40$ kpc, which declines to $\langle\kappa\rangle \approx 24$ per cent at $40 < d < 100$ kpc (through private communication). The steep anticorrelation and the mean covering fraction is roughly consistent with our results, where we find $<\kappa>$ declines from $\langle\kappa\rangle = 0.83^{+0.06}_{-0.05}$ at $d < 40$ kpc to $\langle\kappa\rangle = 0.37^{+0.07}_{-0.07}$ at $d \approx 40$–90 kpc.

It is clear from our results that Mg II absorbing gas is tightly coupled with the physical properties of host galaxies. In particular, our survey displays a strong dependence of mean covering fraction of Mg II absorbing gas $\langle\kappa\rangle$ on the stellar mass of host galaxies, where $\langle\kappa\rangle$ increases with mass at $\log M_{\rm star}/{\rm M}_\odot \lesssim 10.6$ and decreases steeply at higher masses. We further demonstrate in Section 5.2 that at the same stellar masses of $\log\langle M_{\rm star}/{\rm M}_\odot\rangle = 10.55$, star-forming galaxies have in average twice of the mean Mg II gas covering fraction (64 per cent) compared to that of quiescent galaxies (29 per cent). The properties of Mg II absorbing gas are shown to strongly depend on multiple host galaxy properties. Here, we highlight the importance of having a homogeneous, absorption-blind galaxy sample, in order to identify different dependences (e.g. stellar mass and star-formation) and carefully study how Mg II gas correlates with their host galaxy properties.

6 SUMMARY

We have carried out the M3 Halo Project of galaxies and Mg II absorbers in the spectra of background QSOs that are within close projected distances at $z < 0.5$. The catalogue contains 211 isolated and 43 non-isolated galaxy–QSO pairs with spectroscopic redshifts of $\langle z\rangle_{\rm med} = 0.21$ and projected distances of $\langle d\rangle_{\rm med} = 86$ kpc. This is the largest homogeneous, absorption-blind sample at $z \sim 0.2$ to date, allowing us to conduct a comprehensive study of the correlation between Mg II absorbing gas and the physical properties of host galaxies at low-redshift. The main findings of our survey are summarized as the following:

(1) We observe a stark contrast in the distribution of Mg II absorber strength $W_r(2796)$ versus galaxy projected distance d between isolated and non-isolated galaxies (Fig. 4). While both galaxy samples appear to occupy a similar $W_r(2796)$ versus d space, isolated galaxies show strong inverse correlation but non-isolated galaxies exhibit no hint of a trend among detections. When dividing isolated galaxies into star-forming and quiescent galaxy samples, star-forming galaxies show a strong anticorrelation between $W_r(2796)$ and distance d, in contrast to the moderate trend revealed in quiescent galaxy sample.

(2) Based on the likelihood analysis, we confirm that $W_r(2796)$ declines with increasing d for isolated galaxies. The anticorrelation between $W_r(2796)$ and d is strengthened when considering only isolated, star-forming galaxies. The inverse correlation is further enhanced for star-forming galaxies after accounting for either mass scaling of gaseous radius ($R_{\rm h}$), B-band luminosity ($L_{\rm B}$), or stellar mass ($M_{\rm star}$) of host galaxies. On the contrary, Mg II detected quiescent galaxies exhibit little correlation between $W_r(2796)$ and d, whether or not accounting for scaling (see Figs 5 and 6).

(3) In Fig. 7, we show that the covering fraction of Mg II absorbing gas $\langle\kappa\rangle$ is high for isolated galaxies at small projected distances d and declines rapidly to $\langle\kappa\rangle \approx 0$ at $d \gtrsim 100$ kpc for absorbers of $W_r(2796) \geq 0.3$ Å. At $d < 40$ kpc, we find an elevated covering fraction $\langle\kappa\rangle \sim 0.83$ for star-forming galaxies compared to $\langle\kappa\rangle \sim 0.57$ for quiescent galaxies. After the scaling of B-band luminosity, the inverse correlation between $\langle\kappa\rangle$ and d is strengthened and the difference in covering fraction between star-forming and quiescent galaxies become more evident ($\sim 3\sigma$).

(4) The high Mg II gas covering fraction for both our star-forming and quiescent galaxy samples at $d < 90$ kpc ($\langle\kappa\rangle \sim 0.3$–$0.8$) is in stark contrast to what we have seen in the massive LRGs. Within $R_{\rm gas}$, we find a sharp decline of Mg II covering fraction $\langle\kappa\rangle$ from 30–70 per cent around L_* galaxies to 10–15 per cent around massive LRGs (Fig. 8a). The strong mass dependence of Mg II incidence is qualitatively consistent with the expectation from the observed clustering of Mg II absorbers. In addition, at stellar mass of $\log\langle M_{\rm star}/{\rm M}_\odot\rangle \approx 10.6$, the Mg II gas covering fraction for quiescent galaxies ($\langle\kappa\rangle = 0.29$) is merely half of what we find for star-forming galaxies ($\langle\kappa\rangle = 0.64$). We also find a positive correlation between sSFR and Mg II gas covering fraction (Fig. 8b).

(5) We find that most of the galaxy–Mg II absorber pairs have relative velocities smaller than the expected projected escape velocity of their host haloes, implying that the Mg II absorbers are likely to be gravitationally bound (Fig. 9). In addition, Mg II absorbers have line-of-sight velocity dispersion of $\sigma = (58$–$73, 73$–$90)$ km s^{-1} for low-mass and high-mass star-forming galaxies, consistent with the expected line-of-sight velocity dispersion $\sigma = (52, 86)$ km s^{-1} for virialized motion. If the clouds are massive enough to travel through the hot gas at the halo velocity without significant deceleration by the hot gas drag force, we are able to place lower limits on the cloud mass of $m_{\rm cl} \sim 10^5\,{\rm M}_\odot$ and the cool gas accretion rate of ~ 0.7–$2\,{\rm M}_\odot\,{\rm yr}^{-1}$.

(6) In Fig. 11, we investigate the possible azimuthal dependence in the covering fraction of Mg II absorbers for isolated, star-forming and quiescent galaxies. While no apparent trend is seen for quiescent galaxies at $d \leq 0.4\,R_{\rm h}$, there is a modest enhancement in the gas covering fraction along the minor axis of star-forming galaxies at $0.2 < d \leq 0.4\,R_{\rm h}$. We find excess $W_r(2796)$ around galaxies closer to the minor axis ($\Phi \leq 45^\circ$) at $\lesssim 1\sigma$ level. No statistical significant dependence of $<\kappa>_{\rm Mg\,II}$ or $W_r(2796)$ on azimuthal angle Φ is shown in our isolated galaxy sample.

ACKNOWLEDGEMENTS

The authors thank Stephanie Ho for the covering fraction measurement for their survey and careful reading on the early draft of this paper. HWC acknowledges partial support from *HST*-GO-

15163.001A and NSF AST-1715692 grants. YHH acknowledges support from NSF AST 15-15115 and AST 19-08284 grants.

We are grateful to the SDSS collaboration for producing and maintaining the SDSS public data archive. Funding for the SDSS and SDSS-II has been provided by the Alfred P. Sloan Foundation, the Participating Institutions, the National Science Foundation, the U.S. Department of Energy, the National Aeronautics and Space Administration, the Japanese Monbukagakusho, the Max Planck Society, and the Higher Education Funding Council for England. The SDSS Web Site is http://www.sdss.org/. The SDSS is managed by the Astrophysical Research Consortium for the Participating Institutions.

This research has made use of NASA's Astrophysics Data System and the NASA/IPAC Extragalactic Database (NED) that is operated by the Jet Propulsion Laboratory, California Institute of Technology, under contract with the National Aeronautics and Space Administration.

Based on data gathered with the 6.5-m Magellan Telescopes located at Las Campanas Observatory.

DATA AVAILABILITY

The data underlying this article will be shared on reasonable request to the corresponding author.

REFERENCES

Abolfathi B. et al., 2018, ApJS, 235, 42
Adelman-McCarthy J. K. et al., 2008, ApJS, 175, 297
Afruni A., Fraternali F., Pezzulli G., 2019, A&A, 625, A11
Anderson T. W., Darling D., 1952, Ann. Math. Stat., 23, 193
Bacon R. et al., 2010, in McLean I. S., Ramsay S. K., Takami H., eds, Ground-based and Airborne Instrumentation for Astronomy III. Society of Photo-Optical Instrumentation Engineers (SPIE) Conference Series, Vol. 7735, p. 773508
Bergeron J., Stasińska G., 1986, A&A, 169, 1
Bordoloi R. et al., 2014, ApJ, 796, 136
Borthakur S., Heckman T., Strickland D., Wild V., Schiminovich D., 2013, ApJ, 768, 18
Borthakur S. et al., 2016, ApJ, 833, 259
Bryan G. L., Norman M. L., 1998, ApJ, 495, 80
Charlton J. C., Churchill C. W., 1998, ApJ, 499, 181
Charlton J. C., Ding J., Zonak S. G., Churchill C. W., Bond N. A., Rigby J. R., 2003, ApJ, 589, 111
Chen H.-W., 2017, in Knapen J. H., Lee J. C., Gil de Paz A., eds, Astrophysics and Space Science Library, Vol. 434, Outskirts of Galaxies. Springer-Verlag, Berlin, p. 291
Chen H.-W., Mulchaey J. S., 2009, ApJ, 701, 1219
Chen H.-W., Tinker J. L., 2008, ApJ, 687, 745
Chen H.-W., Lanzetta K. M., Webb J. K., Barcons X., 1998, ApJ, 498, 77
Chen H.-W., Helsby J. E., Gauthier J.-R., Shectman S. A., Thompson I. B., Tinker J. L., 2010a, ApJ, 714, 1521 (C10)
Chen H.-W., Wild V., Tinker J. L., Gauthier J.-R., Helsby J. E., Shectman S. A., Thompson I. B., 2010b, ApJ, 724, L176
Chen H.-W., Gauthier J.-R., Sharon K., Johnson S. D., Nair P., Liang C. J., 2014, MNRAS, 438, 1435
Chen H.-W., Boettcher E., Johnson S. D., Zahedy F. S., Rudie G. C., Cooksey K. L., Rauch M., Mulchaey J. S., 2019, ApJ, 878, L33
Chomiuk L., Povich M. S., 2011, AJ, 142, 197
Churchill C. W., Mellon R. R., Charlton J. C., Jannuzi B. T., Kirhakos S., Steidel C. C., Schneider D. P., 2000, ApJS, 130, 91
Churchill C. W., Vogt S. S., Charlton J. C., 2003, AJ, 125, 98
Churchill C. W., Nielsen N. M., Kacprzak G. G., Trujillo-Gomez S., 2013, ApJ, 763, L42
Epinat B. et al., 2018, A&A, 609, A40
Faber S. M. et al., 2007, ApJ, 665, 265
Feigelson E. D., Nelson P. I., 1985, ApJ, 293, 192
Fossati M. et al., 2019, MNRAS, 490, 1451
Fumagalli M. et al., 2012, ApJ, 757, L22
Gauthier J.-R., 2013, MNRAS, 432, 1444
Gauthier J.-R., Chen H.-W., 2011, MNRAS, 418, 2730
Hao J. et al., 2010, ApJS, 191, 254
Ho S. H., Martin C. L., 2020, ApJ, 888, 14
Ho S. H., Martin C. L., Kacprzak G. G., Churchill C. W., 2017, ApJ, 835, 267
Huang Y.-H., Chen H.-W., Johnson S. D., Weiner B. J., 2016, MNRAS, 455, 1713
Johnson S. D., Chen H.-W., Mulchaey J. S., Tripp T. M., Prochaska J. X., Werk J. K., 2014, MNRAS, 438, 3039
Johnson S. D., Chen H.-W., Mulchaey J. S., 2015a, MNRAS, 449, 3263
Johnson S. D., Chen H.-W., Mulchaey J. S., 2015b, MNRAS, 452, 2553
Johnson S. D. et al., 2018, ApJ, 869, L1
Kacprzak G. G., Churchill C. W., Steidel C. C., Murphy M. T., 2008, AJ, 135, 922
Kacprzak G. G., Churchill C. W., Evans J. L., Murphy M. T., Steidel C. C., 2011, MNRAS, 416, 3118
Kacprzak G. G., Churchill C. W., Nielsen N. M., 2012, ApJ, 760, L7
Kewley L. J., Dopita M. A., Sutherland R. S., Heisler C. A., Trevena J., 2001, ApJ, 556, 121
Koester B. P. et al., 2007, ApJ, 660, 239
Kravtsov A. V., Vikhlinin A. A., Meshcheryakov A. V., 2018, Astron. Lett., 44, 8
Lan T.-W., Mo H., 2018, ApJ, 866, 36
Lanzetta K. M., Turnshek D. A., Wolfe A. M., 1987, ApJ, 322, 739
Liang C. J., Chen H.-W., 2014, MNRAS, 445, 2061
Lupton R. H., 1995, http://www.apo.nmsu.edu/35m_operations/35m_manual/Instruments/DIS/DIS_usage.html#Lupton_Manual, accessed (2/23/2021)
Maller A. H., Bullock J. S., 2004, MNRAS, 355, 694
Maller A. H., Berlind A. A., Blanton M. R., Hogg D. W., 2009, ApJ, 691, 394
Marshall J. L. et al., 2008, in McLean I. S., Casali M. M., eds, Proc. SPIE Conf. Ser. Vol. 7014, Ground-Based and Airborne Instrumentation for Astronomy II. SPIE, Bellingham, p. 54
Martin C. L., Ho S. H., Kacprzak G. G., Churchill C. W., 2019, ApJ, 878, 84
Mo H. J., Miralda-Escude J., 1996, ApJ, 469, 589
More S., van den Bosch F. C., Cacciato M., Skibba R., Mo H. J., Yang X., 2011, MNRAS, 410, 210
Navarro J. F., Frenk C. S., White S. D. M., 1997, ApJ, 490, 493
Nestor D. B., Turnshek D. A., Rao S. M., 2005, ApJ, 628, 637
Nielsen N. M., Churchill C. W., Kacprzak G. G., Murphy M. T., 2013a, ApJ, 776, 114
Nielsen N. M., Churchill C. W., Kacprzak G. G., 2013b, ApJ, 776, 115
Nielsen N. M., Kacprzak G. G., Pointon S. K., Churchill C. W., Murphy M. T., 2018, ApJ, 869, 153
Petitjean P., Bergeron J., 1990, A&A, 231, 309
Prochaska J. X., Weiner B., Chen H. W., Mulchaey J., Cooksey K., 2011, ApJ, 740, 91
Rao S. M., Turnshek D. A., Nestor D. B., 2006, ApJ, 636, 610
Rubin K. H. R., Prochaska J. X., Koo D. C., Phillips A. C., Martin C. L., Winstrom L. O., 2014, ApJ, 794, 156
Rudie G. C., Steidel C. C., Shapley A. E., Pettini M., 2013, ApJ, 769, 146
Smith A. G., Hopkins A. M., Hunstead R. W., Pimbblet K. A., 2012, MNRAS, 422, 25
Tinker J. L., Chen H.-W., 2008, ApJ, 679, 1218
Tinker J. L., Chen H.-W., 2010, ApJ, 709, 1
Tinker J. L., Norberg P., Weinberg D. H., Warren M. S., 2007, ApJ, 659, 877
Tripp T. M., Lu L., Savage B. D., 1998, ApJ, 508, 200
Tumlinson J. et al., 2011, Science, 334, 948
Tumlinson J. et al., 2013, ApJ, 777, 59
Tumlinson J., Peeples M. S., Werk J. K., 2017, ARA&A, 55, 389

Wechsler R. H., Bullock J. S., Primack J. R., Kravtsov A. V., Dekel A., 2002, ApJ, 568, 52
Weiner B. J. et al., 2009, ApJ, 692, 187
Werk J. K. et al., 2014, ApJ, 792, 8
Whiting M. T., Webster R. L., Francis P. J., 2006, MNRAS, 368, 341
Yan R., Newman J. A., Faber S. M., Konidaris N., Koo D., Davis M., 2006, ApJ, 648, 281
Yang X., Mo H. J., Jing Y. P., van den Bosch F. C., 2005, MNRAS, 358, 217
Zahedy F. S., Chen H.-W., Rauch M., Wilson M. L., Zabludoff A., 2016, MNRAS, 458, 2423
Zahedy F. S., Chen H.-W., Johnson S. D., Pierce R. M., Rauch M., Huang Y.-H., Weiner B. J., Gauthier J.-R., 2019, MNRAS, 484, 2257
Zheng Z., Coil A. L., Zehavi I., 2007, ApJ, 667, 760
Zhu G., Moustakas J., Blanton M. R., 2009, ApJ, 701, 86
Zhu G. et al., 2014, MNRAS, 439, 3139

SUPPORTING INFORMATION

Supplementary data are available at *MNRAS* online.

suppl_data

Please note: Oxford University Press is not responsible for the content or functionality of any supporting materials supplied by the authors. Any queries (other than missing material) should be directed to the corresponding author for the article.

This paper has been typeset from a TEX/LATEX file prepared by the author.